Mechanical Behavior and Borehole Fracturing of Antarctic Polar Drilling: Experimental and Peridynamic Modeling

Haoran Xu[1,5], Yongsheng Liu [1,2,3,4*], Gansheng Yang [1,2], Bing Li[2], Xiaohui Chen[4], Xiaonan Hou[5]

[1] China University of Geosciences, Beijing, 100083, China

[2] Key Laboratory of Polar Geology and Marine Mineral Resources, Ministry of Education, Beijing, 100083, China

[3] Hainan Institute of China University of Geosciences, Beijing, China

[4] Geomodelling and Artificial Intelligence Centre, School of Civil Engineering, University of Leeds, Leeds LS2 9JT, UK

[5] School of Engineering, Lancaster University, Lancaster, LA1 4YW, UK

*Corresponding author: Yongsheng Liu (yongsheng@cugb.edu.cn)

Abstract

The mechanical behavior and failure mechanisms of Antarctic ice play a key role on borehole stability and structural integrity during polar drilling. Understanding these properties is essential for the design and operation in polar and offshore engineering. Due to long-term natural compaction and formation processes, Antarctic ice exhibits mechanical characteristics that differ from freshwater and sea ice. Existing constitutive models are inadequate for predicting mechanical response of Antarctic ice. This paper focuses on compressive behavior and constitutive relation of real Antarctic ice from polar scientific expedition. Uniaxial and triaxial tests are performed to analyze the effects of loading rate, temperature, and confining pressure. The results show that under

uniaxial compression, increasing loading rates change the failure mode from shear to splitting, reflecting a rate-dependent ductile-brittle behavior. In the triaxial tests, confining pressure suppresses crack propagation, resulting in radial expansion without cracking. Based on experimental results, a constitutive model is developed for Antarctic ice, integrating both the nonlinear elastic and rate-dependent viscoelastic behavior. The proposed model shows excellent predictive accuracy, with peak stress errors below 3.52% and overall trends that matched experimental results ($R^2 > 0.977$). The model is implemented within peridynamics to analyze ice borehole fracturing, highlighting the influence of loading rate on failure evolution. These findings enhance the understanding of Antarctic ice mechanics, providing experimental and theoretical insights for borehole fracturing in polar and offshore drilling.

Keywords: Polar drilling, Antarctic ice, Constitutive model, Peridynamics, Borehole fracturing

1 Introduction

Ice sheets and glaciers cover 11% of the Earth's land surface, with more than 98% of Antarctica and most of Greenland covered by ice. As offshore and polar exploration advances, understanding ice mechanics has become increasingly important for the development of polar infrastructure (Hjort et al., 2022; Bailey et al., 2015), offshore ice-based platforms (Mohapatra et al., 2025; Xu et al., 2020; Zhang et al., 2023)**,** and deep ice drilling (Goodge et al., 2021; Kuhl et al., 2021; Lv et al., 2024). In particular, during polar and oceanic ice drilling operations, ice deformation and fracturing by drilling disturbances directly affect borehole stability. A thorough understanding of the mechanical properties of ice is an important foundation for ensuring the engineering reliability in polar and offshore environments.

Unlike seasonal ice forms such as river and sea ice, polar ice develops over geological

timescales. Antarctic ice is formed through a long-term continuous compaction and recrystallization process of snow. As surface snow builds up over time, the snow layers get pressed down by gravity, slowly turn into glacial ice (Fourteau et al., 2020). This is different from water freezing in normal temperatures, polar ice forms under above and horizontal pressure. This process makes the ice layers have uneven density and pore shapes. Surface ice has larger and irregularly distributed pores, while deeper ice has smaller and more compact pores (Freitag et al., 2004). The mechanical behavior of polar ice is governed by its unique geological processes, influenced by factors such as temperature, pore structure, and stress state. So, the ice has clear differences in space and time at many scales, and this brings challenges for understanding ice strength, fracture, and constitutive modeling.

The mechanical behavior of ice is influenced by its formation history, resulting in distinct strength and deformation characteristics. Marchenko et al. (2013) found that the elastic modulus of ice ranges from 1.7 to 9.1 GPa, showing the high heterogeneity among different ice types. Fracture toughness is a key parameter for crack propagation, and it is dependent on loading rate. Timco & Weeks, (2010) reported that fracture toughness of ice ranges from 115 to 250 $kPa \cdot m^{0.5}$. Snyder et al. (2016) proposed a critical strain rate of ice (10^{-3} s^{-1}) that shows the shift from brittle to ductile deformation. Under slow strain rates, ice shows ductile, while high strain rates lead to brittle fracture. Similar to rock, tensile failure is the dominant pattern for ice (Litwin et al., 2012). Zhang et al. (2020) studied the dynamic splitting tensile of ice using a modified SHPB. They found that tensile strength increases with faster strain rates and colder temperatures, and strain rate shows the greater influence.

In deep geological environments, ice is usually subjected to triaxial stress, exhibiting complex failure behavior. Rist & Murrell, (1994) pointed out that shear forces are the main reason for ice

fracture under triaxial pressure, with shear failure happens on a flat surface cut at 45° to the maximum principal stress. Wang et al. (2018, 2020) studied the axial compression behavior of ice-filled circular steel tubes, providing important insights into ice-structure interaction under lateral confinement. Recently, Xu et al. (2023, 2024) studied borehole failure in complex subglacial environments, revealing the coupled effects on ice failure under different geological conditions. Most research focus on observing and describing macroscopic phenomena, a systematic constitutive framework is still lacking for polar ice to characterize the complex response.

Current constitutive models for ice are not enough to accurately describe mechanical behavior under different stress states. Ince et al. (2017) used empirical constitutive equations to describe the stress-strain relationship of ice, which is difficult to reflect the post-peak softening behavior. Shan et al. (2018) improved the Duncan-Chang model. They enhanced the hyperbolic function with a strain-squared term, allowing it to represent initial compaction and nonlinear stages. However, these models remain empirical fits to experimental data and lack mechanistic insight. Elastic-brittle constitutive model is instantaneous and rate-independent (Girard et al., 2011). In the rheological characterization of ice, there remains debate regarding the validity of plasticity and viscoelastic theory (Mokhtari and Leira, 2024). The plasticity model uses different flow rules, while the viscoelastic model combines elastic and viscous elements. Regarding plasticity models, the crushable foam (CF) model, grounded in the elliptical yield criterion, is extensively applied in icebreaking simulations (Gagnon, 2011; Gagnon and Wang, 2012; Kim and Kim, 2019; Obisesan and Sriramula, 2018). Han et al. (2017) argued that the CF plasticity model improves Drucker-Prager and Mohr-Coulomb models in icebreaking simulations. However, the CF model has a zero plastic Poisson's ratio, limiting its ability to simulate confining pressure effects (Mokhtari and Leira,

2024). By contrast, viscoelastic models offer a clearer representation of physical mechanisms. Dansereau et al. (2016) introduced a viscous damping component into an elastic constitutive to characterize the response of sea ice and rocks. The model captured key features, such as strain localization and anisotropy. However, its reliance on a linear elasticity assumption limits its applicability.

To address these limitations, this paper proposes a novel nonlinear Maxwell constitutive model. The model employs a parallel structure of a nonlinear spring and generalized Maxwell body, combined with a strain-rate power-law relationship. Results show that the proposed model exhibits excellent predictive accuracy on peak stress and overall behavior by uniaxial tests with real Antarctic ice samples.

Owing to Antarctica's unique geographic and climatic conditions, experimental and theoretical research on the mechanical properties of Antarctic ice remain limited. In this paper, Antarctic ice samples were collected during polar scientific expeditions, and the deformation behavior and failure characteristics were analyzed by mechanical testing. Uniaxial and triaxial experiments were conducted in a low-temperature laboratory to study the effects of temperature, confining pressure, and loading rate. Based on generalized Maxwell theory, a constitutive model for real Antarctic ice was proposed and validated. The constitutive model was integrated into peridynamics to simulate ice borehole fracturing, providing theoretical insights for the development of polar drilling engineering.

2 Materials and Methods

2.1 Antarctic ice

The ice crystals are classified into single-crystal and polycrystalline. Single-crystal ice is a type

of ice crystal that forms from a single nucleation site during the freezing or sublimation process, with its molecules arranged in a regular, periodic pattern in three-dimensional space. Single-crystal ice requires high water purity and precise control of heat flow, so most ice in nature is polycrystalline. Polycrystalline ice is a collection of single-crystal ice grains with different orientations of their principal axes, where each ice crystal has a distinct shape and size. Two ice cores, each with a diameter of 9 cm and lengths of 60 cm and 54 cm, as shown in Fig. 1, were drilled and extracted at an elevation of 497 m near the Zhongshan Station in Antarctica (at latitude 69°30′48.87″ S, longitude 76°17′56.63″ E) during China's Antarctic research expedition. Observation of Antarctic ice samples and their cross-sectional slices reveal the presence of numerous bubbles, pores, and impurities.

Fig. 1. Antarctic ice sample.

Glacier ice exhibits variations in polar regions due to different snow accumulation rates, stress distribution, temperature, and recrystallization. The ice's composition is relatively complex, comprising air, salts, and impurities, resulting in diverse and highly complex physical and mechanical properties. Fig. 2 shows the crystal structure of Antarctic ice and plain ice in both

horizontal and vertical cross-sections. Plain ice exhibits anisotropy, with mechanical properties varying depending on the orientation of the crystals. However, Antarctic ice exhibits consistent behavior in both horizontal and vertical directions, making it an isotropic polycrystal.

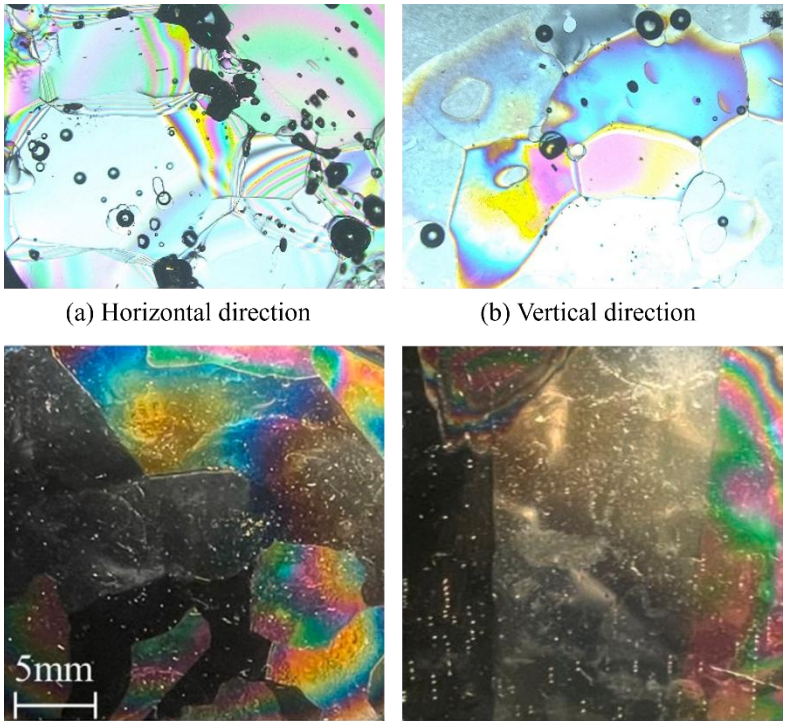

(a) Horizontal direction (b) Vertical direction

(c) Horizontal direction (d) Horizontal direction

Fig. 2. Ice crystal. (a) and (b): Antarctic ice; (c) and (d): Plain ice (Lou and Wu, 2021).

2.2 Low-temperature experiment

To investigate the mechanical properties of Antarctic ice, axial compression tests were conducted on ice samples obtained from Antarctica. There is currently no unified international standard for mechanical testing of natural polar ice cores. This paper referenced the sample processing procedures adopted in the Antarctic ice uniaxial and triaxial compression studies by Skatulla et al. (2022) and Liang et al. (2025). Based on common laboratory practices and the special physical properties of Antarctic ice cores, we have developed a systematic sample preparation procedure. The sample processing, preservation, and experimental process are shown in Fig. 3.

(1) Storage and transportation of ice cores. After drilling at Zhongshan Station, Antarctica, the

ice cores were sealed in thermally insulated containers maintained at -20 °C. The cold chain was maintained throughout transportation to prevent recrystallization and microcrack.

(2) Specimen cutting and geometric shaping. Ice cores were cut using a low-speed saw in a -20 °C cold room to avoid local melting caused by frictional heat. Sections with uniformly distributed bubbles and no macroscopic cracks were preferentially selected for specimen preparation. Specimens were machined into cylinders with a diameter of 40 mm and a height of 80 mm (aspect ratio 2:1) to minimize the influence of end friction constraints on stress distribution. Both end faces were precision-ground flat to ensure uniform load application.

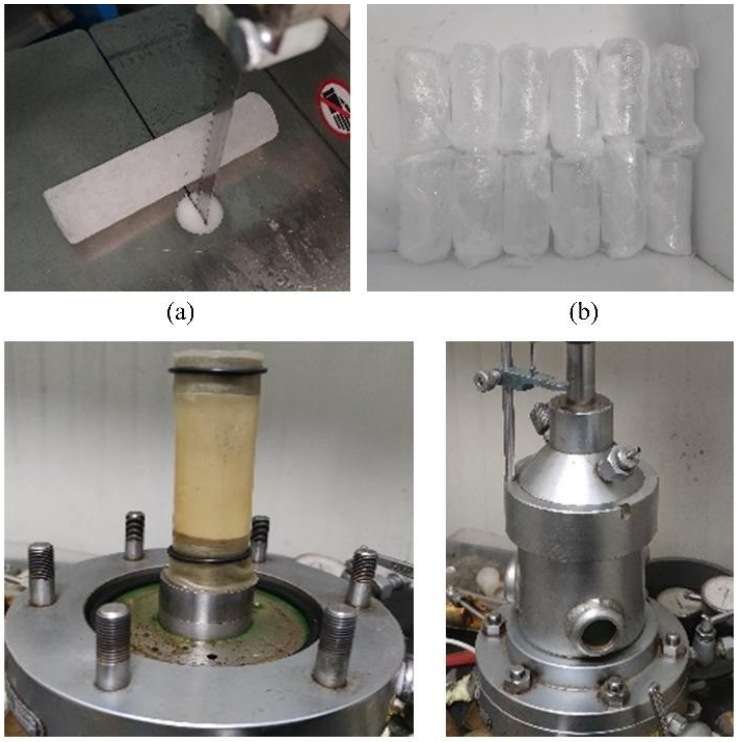

Fig. 3. Ice sample processing, preservation, and experimental process. (a): Sample cutting, (b): Preservation, (c): Wrap latex film, (d): Put ice into the pressure chamber.

(3) Specimen conditioning and temperature equilibration. After cutting, specimens were placed in a low-temperature chamber set to the target experimental temperature (-10 °C or -15 °C) for no less than 24 hours to ensure a fully uniform internal temperature distribution prior to testing.

(4) Encapsulation prior to loading. For triaxial tests, the outer surface of each ice specimen was wrapped with a latex membrane (thickness 0.5 mm) to prevent confining pressure fluid from penetrating the specimen.

A low-temperature environment of -10°C and -15°C was maintained inside the low-temperature test chamber with a well-controlled temperature system. High-precision temperature sensors monitored the temperature variations of the ice samples and the test chamber, and the environmental temperature was adjusted to stay within the range required by the experimental design. At the same time, uniform temperature distribution within the ice samples is essential, as well as avoiding temperature differences between the surface and interior, which could affect the measurement of mechanical properties.

An axial compression testing machine was used to apply pressure to the ice samples. The liquid was injected around the ice sample to apply confining pressure, with the liquid pressure adjusted to control both axial and radial loading pressures, simulating the multi-axial stress state of the ice sample in polar conditions. The stress-strain relationship and failure patterns of the ice samples were studied under different confining pressures. The experimental parameters are shown in **Table 1**. The conversion between loading rate v and strain rate $\dot{\varepsilon}$ is given by $\dot{\varepsilon} = \frac{v}{L_0 \cdot 60}$, L_0 is the specimen gauge length. This converts the loading rate from mm/min to strain rate in s^{-1}.

Table 1. Experimental condition settings.

Number	Size (mm)	Loading rate ($mm \cdot min^{-1}$)	Strain rate (s^{-1})	Temperature (°C)	Confining pressure (MPa)
1	Ø39.9×79.8	1.44	3.00×10^{-4}	-10	0
2	Ø41.0×84.5	2.54	5.00×10^{-4}	-10	0

3	Ø39.7×78.7	3.31	7.00×10^{-4}	-10	0
4	Ø42.1×79.8	4.79	1.00×10^{-3}	-10	0
5	Ø39.6×80.7	0.80	1.65×10^{-4}	-10	1.0
6	Ø39.0×83.2	0.80	1.60×10^{-4}	-10	1.5
7	Ø38.5×76.5	0.80	1.74×10^{-4}	-10	2.0
8	Ø39.0×75.0	0.80	1.78×10^{-4}	-10	2.5
9	Ø38.9×79.5	0.80	1.68×10^{-4}	-15	1.0
10	Ø38.8×79.6	0.80	1.68×10^{-4}	-15	1.5
11	Ø38.8×77.8	0.80	1.71×10^{-4}	-15	2.0
12	Ø38.9×72.7	0.80	1.83×10^{-4}	-15	2.5

3 Results

3.1 Deformation behavior

Fig. 4 presents the results of the uniaxial compression experiment on Antarctic ice. Due to numerous pores within the ice sample, a distinct compaction state occurred at medium loading rates of 2.54 and 3.31 mm/min, as shown in Fig. 4 (b) (c). A linear relationship is observed in the elastic stage following the compaction stage, indicating that the ice deforms within the elastic region, as per Hooke's Law, where stress is proportional to strain. When the stress reaches the linear elastic limit, the ice sample begins to gradually transition into the nonlinear deformation. The softening stage is characterized by a decrease in stress, which is related to changes in the ice's microstructure and the generation and propagation of cracks. At a loading rate of 4.79 mm/min, the ice ultimately undergoes brittle fracture, accompanied by significant strain localization, resulting in the fragmentation of the ice block.

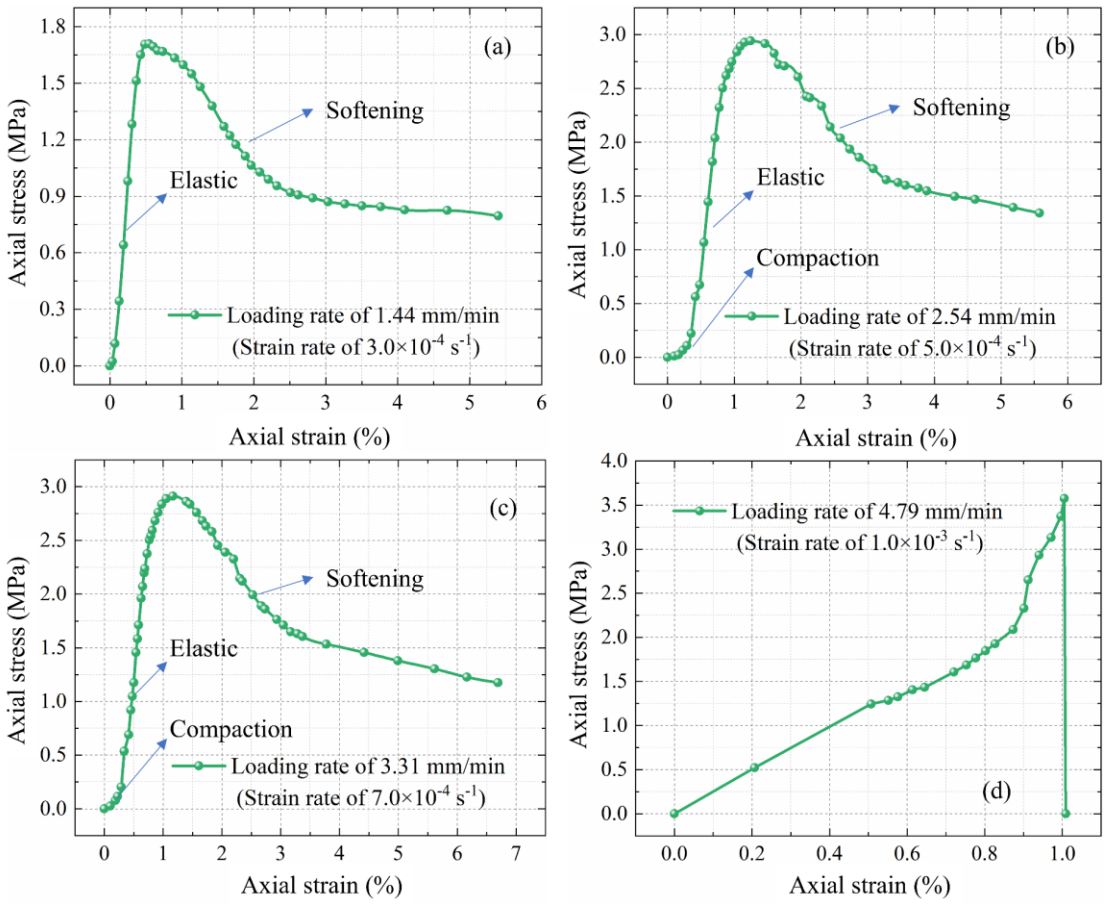

185

186 **Fig. 4.** Axial stress-strain curves under different strain rates

187 Fig. 5 shows the variation in peak and residual strength at different loading rates. The peak

188 strength changes with the loading rate, with a linear correlation coefficient of 0.93. From 1.44 to

189 4.79 mm/min, the peak compressive strength increased by 108.77%. Following a quadratic pattern,

190 the residual strength rises first and then decreases with loading rate. The residual strength of ice is

191 maximized at moderate loading rate. At lower loading rates, the peak strength is reduced, which

192 leads to a lower residual strength. High loading rates crush the ice sample, causing complete failure.

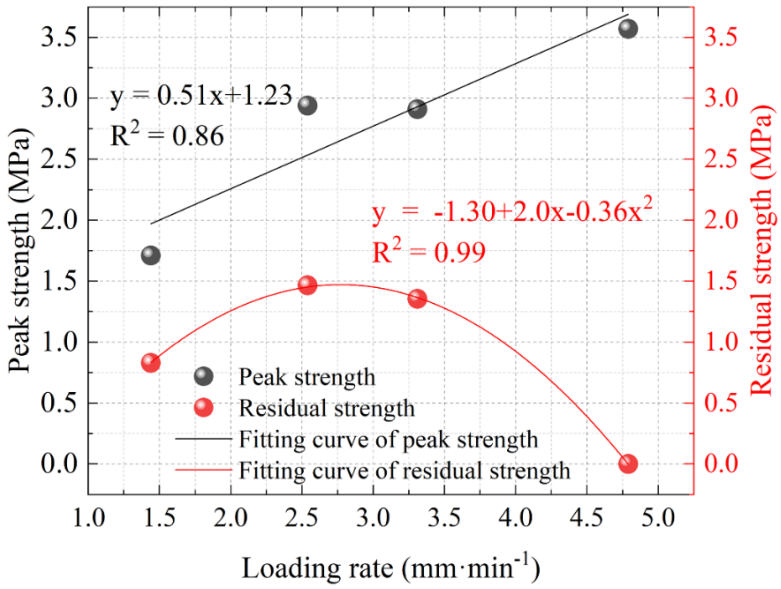

Fig. 5. Peak and residual strength at different loading rates.

Although the limited sample size precludes quantitative error estimation, the experimental results are in good agreement with existing literature data in terms of magnitude and trend. At -10 °C and a strain rate of 3.0×10^{-4} s^{-1}, the compressive strength measured in this study is 1.71 MPa, which is close to the value of 1.886 MPa reported by Liang et al. (2025) for Antarctic ice. At a strain rate of 1×10^{-3} s^{-1}, the measured strength of 3.57 MPa falls within the range of 1.2 - 4.5 MPa reported by Skatulla et al. (2022), providing external validation of the experimental data. The ice cores are precious and irreplaceable natural samples. Only a single specimen was tested for each condition, which is a widely recognized objective limitation in polar ice mechanical research. Single-specimen data may affect the statistical representativeness of the identified model parameters. However, this limitation does not affect the applicability of the proposed constitutive model and peridynamic framework.

Compared to uniaxial experiments, triaxial experiments can more comprehensively simulate the stress conditions that ice experiences in real environments, particularly its behavior under underground multiaxial stress fields, which reflect the rheological properties, yielding behavior, and

fracture patterns of ice. Fig. 6 shows the triaxial stress-strain curves of the ice sample under different confining pressures and temperatures. In the initial phase of the stress-strain curve, the ice sample exhibits linear elastic deformation. The stress is proportional to the strain, indicating that the deformation of the ice is recoverable. As strain increases, the stress-strain relationship of the ice exhibits nonlinearity. The microstructure of the ice undergoes localized changes, with crack initiation or increased internal friction. After entering the softening stage, the curve shows a decrease in stress, which is less pronounced than in the uniaxial test due to the additional confining pressure.

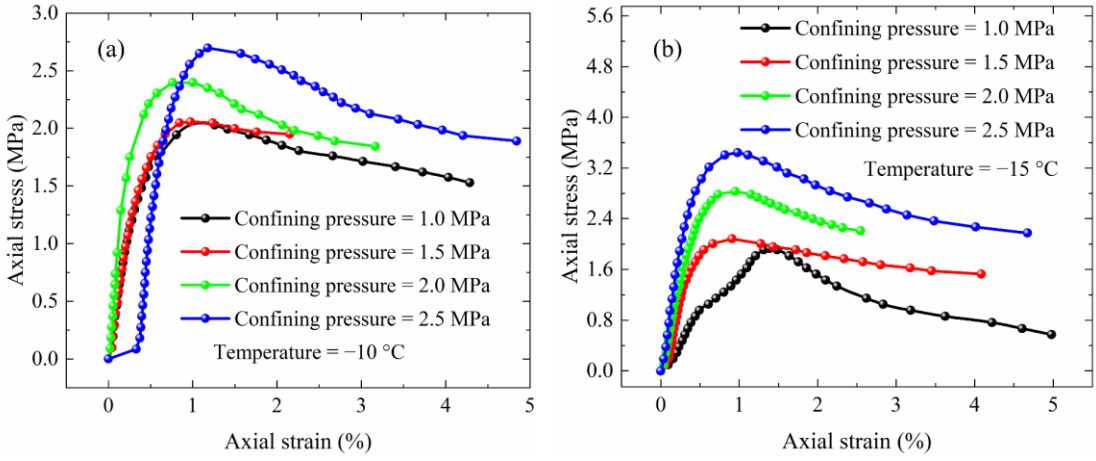

Fig. 6. Axial stress-strain curves of ice samples under different confining pressures and temperatures. (a) -10 ℃, (b) -15 ℃.

Fig. 7 presents the test results under various temperature and confining conditions. The enhancing effect of temperature reduction (from -10 °C to -15 °C) on peak strength is not uniform across all confining pressures, but increases significantly with increasing confining pressure. The specific increments at each confining pressure are as follows: at 1.0, 1.5, 2.0, and 2.5 MPa, the peak strength increments are -4.93%, 0.97%, 16.94%, and 27.41%, respectively, as shown in Fig. 7. This reveals a pattern in which the temperature effect is weak at low confining pressures and becomes pronounced at high confining pressures.

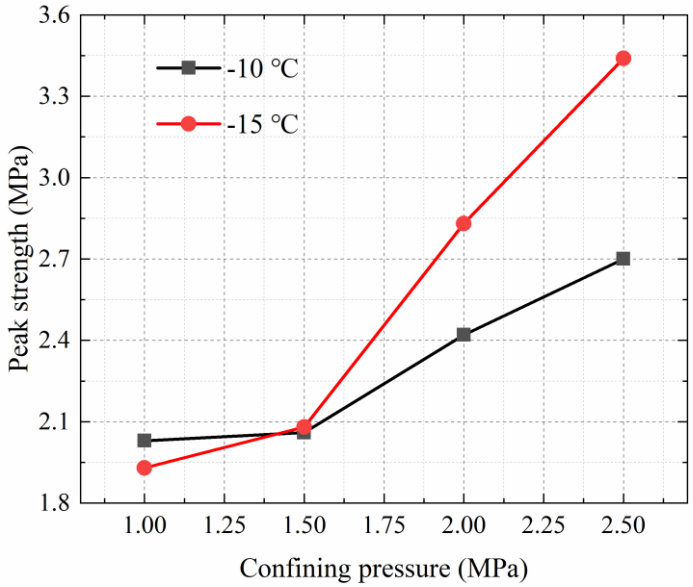

Fig. 7. Peak strength of ice samples affected by confining pressure and temperature.

At low confining pressures (1.0 and 1.5 MPa), failure is dominated by tensile crack propagation. The 5 °C temperature difference produces limited changes in grain boundary strength and crack propagation resistance, resulting in a small temperature effect on peak strength, with differences between the two temperatures remaining within 5%. At high confining pressures (2.0 and 2.5 MPa), tensile crack propagation is suppressed and the deformation mechanism gradually transitions to shear sliding and viscous flow. Viscous deformation is more sensitive to temperature. Lower temperatures increase resistance to dislocation motion in ice crystals and significantly raise grain boundary viscosity, thereby substantially enhancing the overall load-bearing capacity. The strengthening effect induced by the temperature drop from -10 °C to -15 °C is more pronounced at high confining pressures, reaching a maximum increment of 27.41%.

3.2 Failure pattern

The ice samples exhibit a shear-tensile combined failure pattern under lower loading rates of 1.44 and 2.54 mm/min, as shown in Fig. 8. The ice samples exhibit pure tensile longitudinal cracking

failure at higher loading rates of 3.31 and 4.79 mm/min. As the loading rate increases, the ice sample gradually transitions from shear failure to tensile failure.

Fig. 8. Uniaxial compression failure pattern of Antarctic ice samples.

Under low loading rates, the deformation process of Antarctic ice is slower, and time effects influence the crack propagation. Crack propagation is accompanied by shear deformation, where the internal structure of the ice gradually undergoes localized slipping and extension, resulting in a dominant role for shear failure. Under high loading rates, the deformation of the ice sample is primarily characterized by brittle failure, where the stress state of the ice rapidly accumulates, resulting in a dominant longitudinal splitting pattern as shown in Fig. 8 (c) (d). At this point, the strain energy of the ice sample is primarily released through longitudinal cracking.

Fig. 9 shows the triaxial compression failure pattern of the Antarctic ice sample. The ice sample does not exhibit macroscopic through-cracks, except for some radial expansion observed on the outer surface. Under the effect of confining pressure, the external stress on the ice sample is evenly

distributed, reducing crack propagation along the main axis direction. As the confining pressure increases, localized compressive deformation occurs within the ice. These deformations gradually expand, causing dislocation or damage between the microstructure and the grains within the ice sample. The confining pressure suppresses crack propagation, making it more difficult for cracks to propagate along the central compression axis, which leads to a transition in the failure pattern of the ice sample from tensile failure to radial expansion.

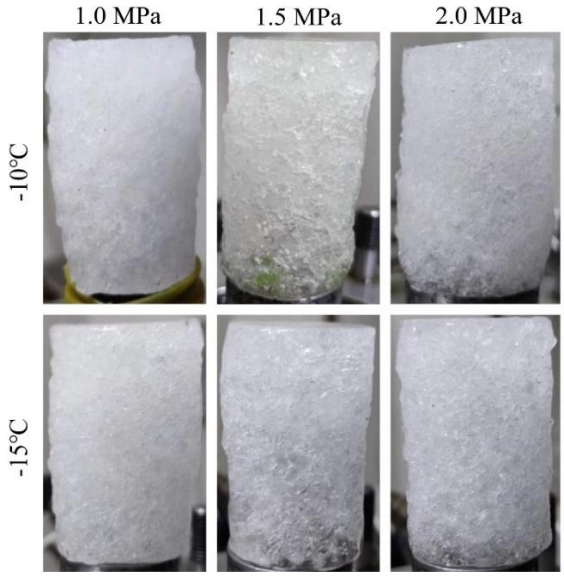

Fig. 9. Triaxial compression failure pattern of Antarctic ice samples.

4 Discussion

4.1 Rate-dependent constitutive model of Antarctic ice

A constitutive model was developed to describe the deformation behavior of Antarctic ice. The model combines nonlinear elasticity with a generalized Maxwell element of linear springs and dashpots. The total stress is expressed as the sum of elastic and viscoelastic components. This allows the model to capture nonlinear elastic evolution and multi power-law viscoelastic mechanism.

The constitutive model for Antarctic ice consists of a nonlinear spring in parallel with a generalized Maxwell body, as shown in Fig. 10. This coupling originates from the iso-strain

condition of the parallel rheological structure. The nonlinear spring and the Maxwell body share the same strain field:

$$\varepsilon_{spring}(t) = \varepsilon_{maxwell}(t) = \varepsilon(t) \tag{1}$$

The parallel model follows the stress superposition principle. The total stress is given by:

$$\sigma_{total}(t) = \sigma_{spring}(\varepsilon(t)) + \sigma_{maxwell}(\varepsilon(t), \dot{\varepsilon}(t)) \tag{2}$$

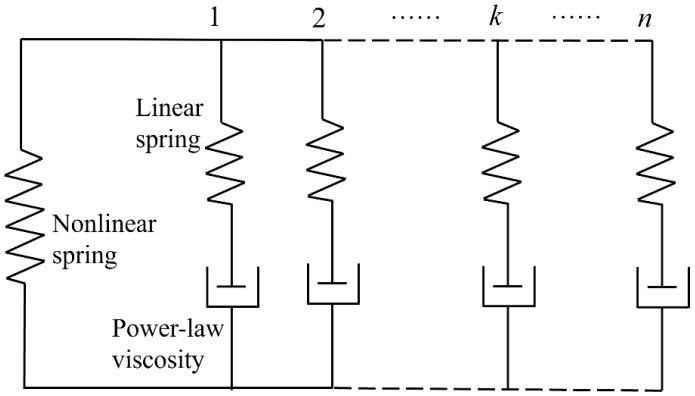

Fig. 10. Parallel connection of nonlinear elasticity and generalized Maxwell elements.

The iso-strain condition ensures kinematic compatibility between the two branches, which is the prerequisite for the coupling. The nonlinear spring describes the instantaneous recoverable elastic energy storage of ice, while the Maxwell element characterizes the rate-dependent viscous dissipation. The two branches are naturally coupled through the shared strain field, and the total stress is their sum. This is the standard mechanical assumption for parallel rheological models. The stress superposition is kinematically self-consistent and requires no additional constraint equations.

The nonlinear elastic element uses improved Duncan-Chang model (Qiu & Peng, 2021; Shan et al., 2018; Zhang et al., 2022). The nonlinear stress-strain relation and its Taylor expansion are given as:

$$\sigma_{spring} = \frac{\varepsilon + d\varepsilon^2}{a + b\varepsilon + c\varepsilon^2} = E_{s0}\varepsilon + E_{s1}\varepsilon^2 \tag{3}$$

where E_{s0} is initial elastic modulus, and $E_{s1}=\frac{1}{a}\left(d-\frac{b}{a}\right)$ is nonlinear modulus, a is instantaneous stiffness of ice at small strains, b controls the weight of the linear term in the denominator. It reflects the activity of ice microdefects during initial loading, such as cracks and grain boundary sliding. Parameter c governs strain softening at larger deformations. It corresponds to progressive softening caused by damage accumulation, including dynamic recrystallization and microcrack propagation. Parameter d controls nonlinear elastic hardening. It reflects stiffness recovery due to lattice hardening or microcrack closure.

Differentiating the nonlinear stress Eq. (3):

$$\frac{\mathrm{d}\sigma}{\mathrm{d}\varepsilon}=\frac{a+2ad\varepsilon+bd\varepsilon^2-c\varepsilon^2}{\left(a+b\varepsilon+c\varepsilon^2\right)^2} \tag{4}$$

At the initial stage, as the strain approaches zero, the initial elastic modulus is given by:

$$E_{s0}=\lim_{\varepsilon\to 0}\frac{\mathrm{d}\sigma}{\mathrm{d}\varepsilon}=\frac{1}{a} \tag{5}$$

The nonlinear spring represents the instantaneous elastic deformation of ice. It serves as an instantaneous response unit, corresponding to the sharp stress rise at the early stage of loading. The Maxwell element acts as a delayed response unit. It describes the stress-strain evolution of rate-dependent ice.

The single Maxwell element consists of a linear spring and a dashpot connected in series. The constitutive relation for the linear spring and dashpot of the k^{th} Maxwell element is given by:

$$\sigma_{ks}=E_k\varepsilon_{ks} \tag{6}$$

$$\sigma_{kv}=\eta_k\dot{\varepsilon}_{kv} \tag{7}$$

where E_k is the elastic modulus of the k^{th} Maxwell element, reflecting the energy storage capacity of the ice lattice. η_k is the viscosity coefficient. ε_{ks} denotes the strain in the spring, and ε_{kv}

309 denotes the strain in the dashpot.

310 The stress equilibrium and strain decomposition of the Maxwell element are as follows:

311 $$\sigma_k = \sigma_{ks} = \sigma_{kv} \tag{8}$$

312 $$\varepsilon = \varepsilon_{ks} + \varepsilon_{kv} \tag{9}$$

313 By combining Eqs. (6), (7), (8), and (9) and differentiating with respect to time, the strain

314 differential form of the k^{th} Maxwell element can be obtained:

315 $$\dot{\varepsilon} = \dot{\varepsilon}_{ks} + \frac{\sigma_{kv}}{\eta_k} = \frac{\dot{\sigma}_{ks}}{E_k} + \frac{\sigma_{kv}}{\eta_k} \tag{10}$$

316 By defining the relaxation time $\theta_k = \eta_k / E_k$ and rewriting the expression into a standard first-

317 order linear differential equation, the stress of the k^{th} Maxwell element can be obtained:

318 $$\dot{\sigma}_k(t) + \frac{1}{\theta_k}\sigma_k(t) = E_k\dot{\varepsilon}(t) \tag{11}$$

319 Both sides of Eq. (11) are multiplied by the integrating factor $\mu(t) = e^{t/\theta_k}$:

320 $$e^{t/\theta_k}\dot{\sigma}_k(t) + \frac{1}{\theta_k}e^{t/\theta_k}\sigma_k(t) = E_k e^{t/\theta_k}\dot{\varepsilon}(t) \tag{12}$$

321 $$\frac{\mathrm{d}}{\mathrm{d}t}\left[e^{t/\theta_k}\sigma_k(t)\right] = E_k e^{t/\theta_k}\dot{\varepsilon}(t) \tag{13}$$

322 After integrating Eq. (13):

323 $$e^{t/\theta_k}\sigma_k(t) = E_k\int_0^t e^{\tau/\theta_k}\dot{\varepsilon}(\tau)\mathrm{d}\tau + \mathrm{C} \tag{14}$$

324 With an initial stress of zero, the integration constant C=0.

325 $$\sigma_k(t) = E_k e^{-t/\theta_k}\int_0^t e^{\tau/\theta_k}\dot{\varepsilon}(\tau)\mathrm{d}\tau = E_k\int_0^t e^{-(t-\tau)/\theta_k}\dot{\varepsilon}(\tau)\mathrm{d}\tau \tag{15}$$

326 Eq. (15) is the stress integral of relaxation kernel function for a single Maxwell element.

327 To characterize the strain rate-dependent behavior of Antarctic ice, this model introduces

328 nonlinear corrections to the dashpot component of the Maxwell element. These modifications

capture the dynamic effects associated with strain rate.

$$\sigma_k(t) = E_k \int_0^t \left(\dot{\varepsilon}(\tau)\right)^m e^{-(t-\tau)/\theta_k} \mathrm{d}\tau \tag{16}$$

where m is the strain rate sensitivity exponent, which dynamically adjusts the dashpot resistance.

The generalized Maxwell stress for multiple elements in parallel is given by:

$$\sigma_{maxwell}(t) = \sum_{k=1}^{n} \sigma_k(t) = \int_0^t \left(\dot{\varepsilon}(\tau)\right)^m \left(\sum_{k=1}^{n} E_k e^{-(t-\tau)/\theta_k} \right) \mathrm{d}\tau \tag{17}$$

This model captures the strain-softening behavior of Antarctic ice by incorporating nonlinear elasticity and rate-dependent effects. The final constitutive equation is expressed as:

$$\sigma(t) = E_{s0}\varepsilon + E_{s1}\varepsilon^2 + \int_0^t \left(\dot{\varepsilon}(\tau)\right)^m \left(\sum_{k=1}^{n} E_k e^{-(t-\tau)/\theta_k} \right) \mathrm{d}\tau \tag{18}$$

The constitutive Eq. (18) is discretized. In the temporal domain, it is expressed as:

$$t_i = (i-1)\Delta t, \quad \Delta t = \frac{\varepsilon_{max} - \varepsilon_{min}}{(n-1)\dot{\varepsilon}_0} \tag{19}$$

The strain rate is calculated using the central difference scheme:

$$\dot{\varepsilon}_i = \begin{cases} \dfrac{\varepsilon_2 - \varepsilon_1}{\Delta t} & i = 1 \\ \dfrac{\varepsilon_{i+1} - \varepsilon_{i-1}}{2\Delta t} & 1 < i < n \\ \dfrac{\varepsilon_n - \varepsilon_{n-1}}{\Delta t} & i = n \end{cases} \tag{20}$$

The relaxation modulus kernel function of the generalized Maxwell body is discretized as:

$$K(i,j) = \sum_{k=1}^{n} E_k \exp\left(-\frac{(i-j)\Delta t}{\theta_k} \right), \quad j \le i \tag{21}$$

The Maxwell integral is finally discretized as follows:

$$\sigma_{maxwell}(i) = \sum_{j=1}^{i-1} \left(\dot{\varepsilon}_j\right)^m K(i,j)\Delta t \tag{22}$$

Parameters are identified by solving a regularized nonlinear least-squares problem using the Trust-Region-Reflective algorithm implemented via the lsqnonlin function in MATLAB:

$$\min_{\mathbf{p}} \mathrm{F}(\mathbf{p}) = \sum_{i=1}^{N} \left(\sigma_i^{\mathrm{model}}(\mathbf{p}) - \sigma_i^{\mathrm{exp}} \right)^2 + \lambda \|\mathbf{p}\|^2 \tag{23}$$

where $\sigma_i^{\mathrm{model}}$ is the model-predicted stress, σ_i^{exp} is the experimentally measured stress, N is the number of data points, and $\lambda = 10^{-6}$ is the regularization coefficient. The regularization term is introduced to prevent overfitting and ensure numerical stability. The convergence tolerance is set to 10^{-6} and the maximum number of iterations is 100.

The strain rate at each time step is approximated using a central difference scheme. The relaxation kernel $K(i, j)$ is precomputed to improve computational efficiency. The initial values of the relaxation times are set at logarithmically equal intervals spanning four decades, so as to capture the viscoelastic response of Antarctic ice across different timescales.

The identified parameter values are listed in Table 2 under four different strain rates.

Table 2. Model parameter identification.

Model parameters	Strain rate of 3×10^{-4} s^{-1}	Strain rate of 5×10^{-4} s^{-1}	Strain rate of 7×10^{-4} s^{-1}	Strain rate of 1×10^{-3} s^{-1}
a	0.0037	0.0182	0.0135	0.0074
b	-0.5900	-2.6248	-2.0650	-1.1434
c	120.39	168.24	151.58	40.55
d	49.41	146.03	137.14	-99.11
E_{s0}	270.27	54.95	74.07	135.14
E_{s1}	56451.21	15947.79	21489.11	7487.37
E_1	10.061	10	10	100.39
E_2	10.058	10	10	100.02
E_3	10.054	10	10	100.28
E_4	10.049	10	10	100.35
E_5	28.872	10	10	100.35
θ_1	0.0003	0.0986	0.0873	1.183

θ_2	0.0001	0.01	0.01	1.6063
θ_3	0.0001	0.001	0.001	0.9958
θ_4	0.0001	0.0001	0.0001	0.9786
θ_5	11.318	0.00001	0.00001	0.9502
m	1.0	0.8	0.8	1.5

4.2 Constitutive model validation

To evaluate the proposed nonlinear generalized Maxwell constitutive model, axial compression test results of Antarctic ice under four different strain rates (3×10^{-4} s^{-1}, 5×10^{-4} s^{-1}, 7×10^{-4} s^{-1} and 1×10^{-3} s^{-1}) were analyzed. To highlight the advantages of the proposed model, the improved Duncan-Chang model (Qiu & Peng, 2021; Shan et al., 2018; Zhang et al., 2022) was used as a comparison. The proposed model demonstrated excellent fitting performance across all strain rate conditions, with coefficients of determination of 0.985, 0.983, 0.984, and 0.977, respectively, as shown in Fig. 11.

Three error metrics are used to evaluate model prediction accuracy:

(1) Coefficient of Determination R^2 : evaluates the goodness of fit of the model to the overall stress-strain curve:

$$R^2 = 1 - \frac{\sum_i (\sigma_i^{exp} - \sigma_i^{model})^2}{\sum_i (\sigma_i^{exp} - \bar{\sigma}^{exp})^2} \tag{24}$$

A value closer to 1 indicates better agreement with the experimental curve.

(2) Relative Error of Peak Stress RE_{peak} : evaluates the prediction accuracy of peak stress:

$$RE_{peak} = \left| \frac{\sigma_{peak}^{model} - \sigma_{peak}^{exp}}{\sigma_{peak}^{exp}} \right| \times 100\% \tag{25}$$

(3) Maximum Relative Error at the steady-state stage MRE_{ss} : evaluates prediction accuracy at the steady-state stage:

$$MRE_{ss} = \max_{i \in steady-state} \left| \frac{\sigma_i^{model} - \sigma_i^{exp}}{\sigma_i^{exp}} \right| \times 100\% \quad (26)$$

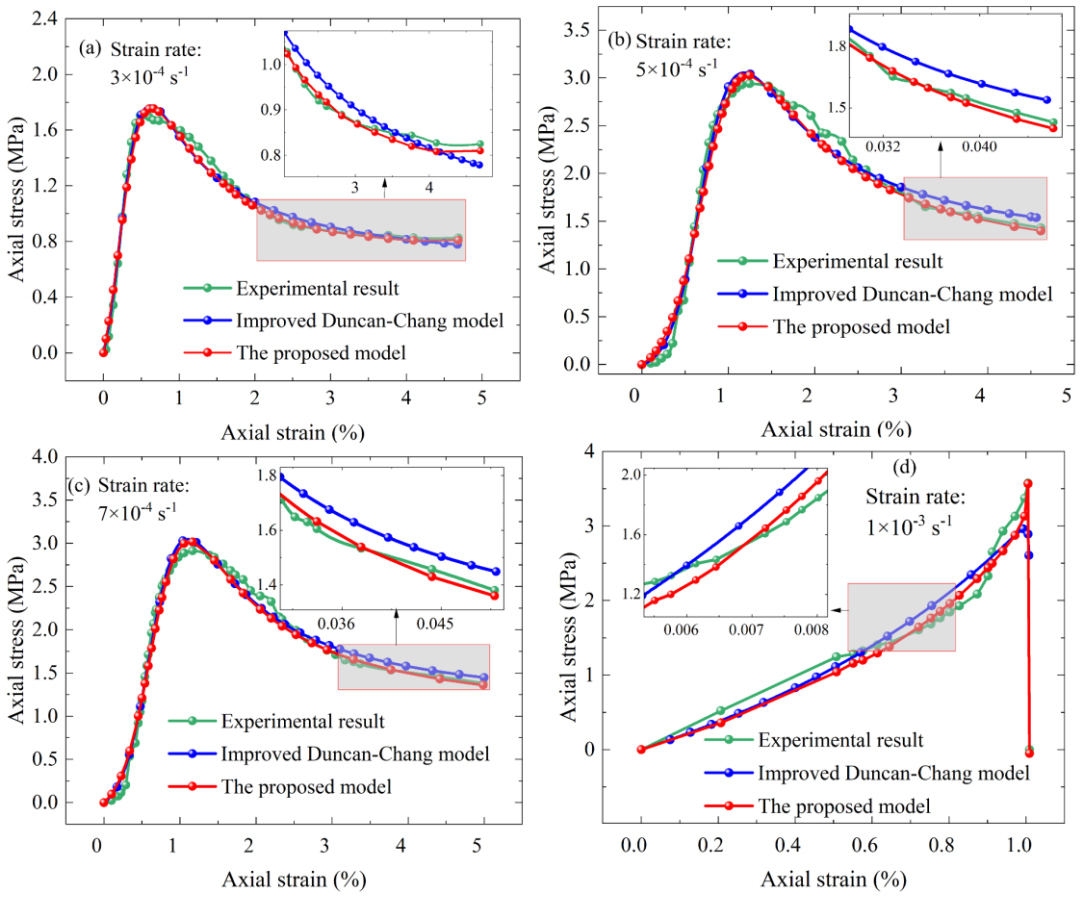

Fig. 11. Comparison of the stress-strain curves by the proposed model with uniaxial experimental results and the improved Duncan-Chang model. An enlarged local view is included, with the coordinate axes aligned with those of the main figure. (a) - (d): strain rates of 3×10^{-4} s^{-1}, 5×10^{-4} s^{-1}, 7×10^{-4} s^{-1} and 1×10^{-3} s^{-1}.

The proposed model accurately captures the key features of the experimental results, including the initial elastic response phase, the gradual softening following peak stress, and the final steady-state flow stage. At a strain rate of 5×10^{-4} s^{-1}, the proposed model reduces the maximum relative error (MRE) in the steady-state stage by 5.36 percentage points compared to the improved Duncan-Chang model. Under high strain rates (1×10^{-3} s^{-1}), experimental observations reveal a brittle failure

mode characterized by an abrupt stress drop after peak stress, without a clear softening transition. The model accurately predicts the peak stress ($RE_{peak} < 3.52\%$) and reproduces the sudden stress drop associated with high strain rate fracture.

4.3 Model characteristic analysis

(1) Strain rate sensitivity

To evaluate strain rate sensitivity of the proposed constitutive model, stress-strain curves are analyzed under eight strain rates, as shown in Fig. 12. As the strain rate increases from 2.5×10^{-5} s^{-1} to 1×10^{-3} s^{-1}, the peak and residual stress increasing by 31.99% and 188.14%.

At initial loading, the Maxwell stress is zero, and ice shows a purely elastic response:

$$\sigma_{maxwell}(t) = \int_0^t \left(\dot{\varepsilon}(\tau)\right)^m \left(\sum_{k=1}^{n} E_k e^{-(t-\tau)/\theta_k} \right) \mathrm{d}\tau = 0 \tag{27}$$

$$\sigma_{total} = \sigma_{spring} = E_{s0}\varepsilon + E_{s1}\varepsilon^2 \tag{28}$$

As time progresses, the effect of Maxwell elements increases, resulting in a stronger strain-rate sensitivity. Ice shows different softening behaviors under different strain-rate ranges. At low strain rates ($< 2 \times 10^{-4}$ s^{-1}), ice softens quickly. At higher strain rates ($> 6 \times 10^{-4}$ s^{-1}), ice exhibits progressive softening. In the transitional strain-rate range, ice shows a mixed softening mode. With increasing strain rate, peak and residual strength of ice increase significantly, reflecting the strain-rate strengthening effect of ice crystals.

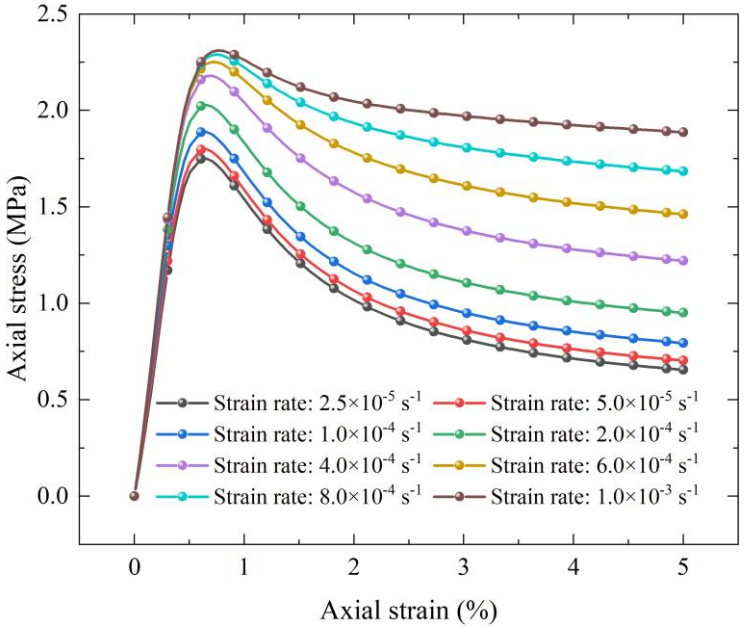

403

404 **Fig. 12.** Axial stress-strain curves at different strain rates.

405 The model accurately reproduces the mechanical response of ice during the strain-softening

406 stage, and captures the deformation behavior of polar ice over different timescales.

407 **(2) Power law index of Maxwell element**

408 The strain rate exponent m introduced in the power-law dashpot is physically rooted in the

409 dislocation creep theory of ice crystals. The plastic flow of ice generally follows Glen's flow law

410 (Glen, 1955):

411 $$\dot{\varepsilon} = A\sigma^n \tag{29}$$

412 where n is the stress exponent and A is a temperature-dependent flow parameter (Goldsby and

413 Kohlstedt, 2001). Rewriting this as a stress-strain rate relationship gives:

414 $$\sigma \propto \dot{\varepsilon}^{1/n} = \dot{\varepsilon}^m, \quad m = \frac{1}{n} \tag{30}$$

415 Therefore, m is essentially the inverse of the stress exponent in Glen's flow law, reflecting the

416 sensitivity of ice crystals to strain rate.

417 To deeply clear the effects of power-law index m in Maxwell element, we analyzed ice

mechanical behavior with m ranging from 0.6 to 1.2 under a strain rate of 1×10^{-4} s^{-1}. Fig. 13 shows theoretical stress-strain curves for different m values. The peak stress exhibits a pronounced dependence on the power-law index, as m increases from 0.6 to 1.2, the peak stress decreases by approximately 37.20%. When m exceeds 0.8, the decline rate in peak stress slows markedly. The residual strength at $m = 0.6$ is 2.62 times higher than that at $m = 1.2$. Both the peak and residual strengths exhibit attenuation that follows a power-law relationship, as illustrated in Fig. 14.

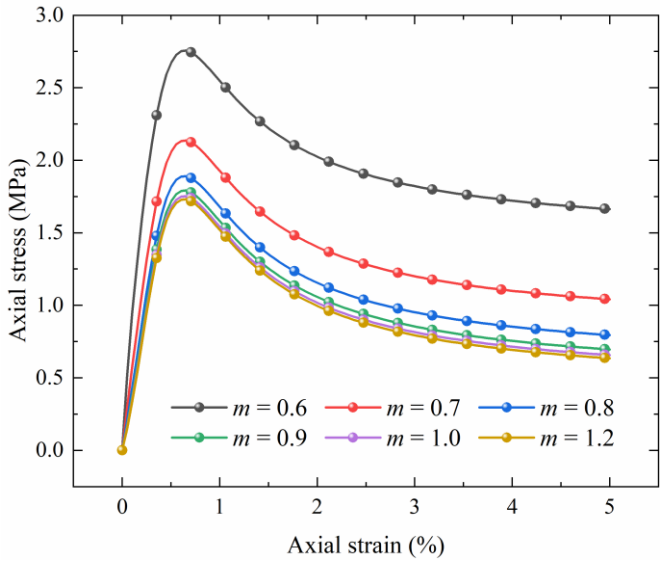

Fig. 13. Theoretical axial stress-strain curves corresponding to different power-law indices (*m* values).

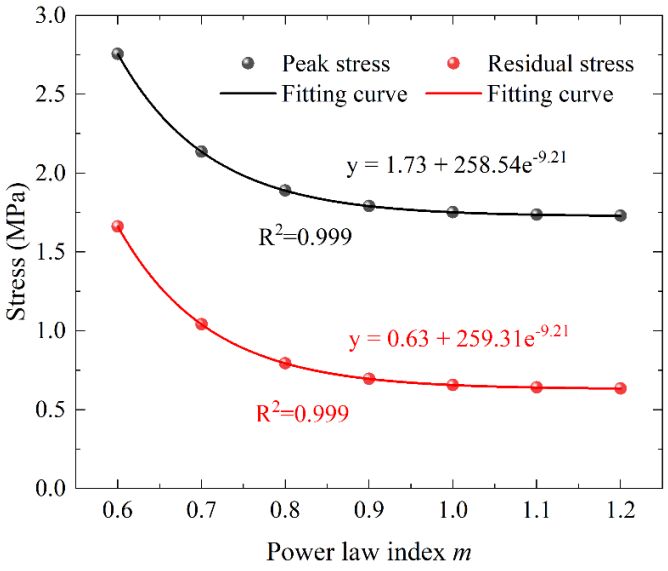

Fig. 14. Decay trends of peak and residual strengths.

The physical essence of the power-law index lies in its role in controlling the nonlinear coupling between stress and viscous strain, which directly influences the rate sensitivity of the Maxwell element. In the sub-linear regime ($m<1$), the viscous stress term $\dot{\varepsilon}^m$ is large and viscous dissipation is highly active. From a microscopic perspective, dislocation motion and grain boundary sliding participate fully in deformation. Strain energy is gradually dissipated through continuous viscous flow, making it difficult for cracks to accumulate sufficient elastic strain energy to drive propagation. The material therefore exhibits ductile deformation with gradual post-peak softening. At $m=1$, the dashpot degenerates into linear viscous flow, corresponding to steady-state creep governed by grain boundary diffusion. In the super-linear regime ($m>1$), the viscous stress term $\dot{\varepsilon}^m$ is small and viscous dissipation channels are suppressed. The contribution of dislocation motion and grain boundary sliding to strain energy consumption is reduced, and elastic strain energy accumulates rapidly at grain boundaries and defect sites. Once the local elastic strain energy exceeds the fracture toughness of ice, microcracks nucleate and propagate rapidly, producing brittle fracture behavior.

4.4 Numerical implementation of Antarctic ice failure

The constitutive model for Antarctic ice encounters key challenges in simulating drilling-induced fractures with complex crack paths. To address the limitations of classical continuum mechanics in discontinuity modeling (Silling and Askari, 2005), peridynamics (PD) is adopted for numerical implementation.

PD theory is a nonlocal approach that utilizes integral equations to describe the behavior of discontinuous region within a unified framework. This approach effectively avoids the singularities commonly encountered in differential equations at material discontinuities (Askari et al., 2008;

Javili et al., 2019; Silling, 2000), demonstrating excellent modeling capabilities and mechanical adaptability. Therefore, the proposed constitutive model is embedded within the PD framework to address ice borehole failure problems involving discontinuous damage.

PD is a mechanical framework grounded in nonlocal theory, wherein a continuum is discretized into points. According to the nonlocal interaction, the PD motion can be written as (Silling, 2000):

$$\rho(x)\ddot{\boldsymbol{u}}(x,t)=\int_H \boldsymbol{f}dV_{x'}+\boldsymbol{b}(x,t) \tag{31}$$

where $\boldsymbol{f}$ denotes the force function between material points, and is governed by the nonlinear spring and Maxwell element. H defines the horizon domain.

Since the constitutive model adopts a parallel structure of a nonlinear spring and a generalized Maxwell body, the total stress satisfies the superposition principle. The corresponding total bond force in the PD framework satisfies the same superposition:

$$f = f_{nonlinear\_spring} + f_{Maxwell} \tag{32}$$

This is the bond-level equivalent of the stress superposition in classical continuum mechanics, and its validity is guaranteed by the iso-strain condition of the parallel structure.

The derivation is based on the plane strain assumption, in which the strain along the borehole axis (z-direction) is zero ($\varepsilon_{33}=0$). Deformation occurs only within the two-dimensional cross-section perpendicular to the borehole axis. Under the plane strain assumption, the three-dimensional strain energy density reduces to a two-dimensional form involving only the in-plane strain components ε_{11} , ε_{22} , and ε_{12} . Since the bond-based PD framework is adopted, bond forces act only along the bond direction. The contribution of the shear strain component ε_{12} to the bond stretch vanishes naturally under the bond-based PD assumption and does not appear explicitly in the strain energy expression. The strain energy density retains only the contributions of ε_{11} and ε_{22} . This is

a direct result of the bond-based PD framework under the plane strain assumption.

(1) Nonlinear spring

The strain energy density associated with the nonlinear spring constitutive relation Eq. (3) in classical continuum mechanics is given by:

$$W_{CCM}(\varepsilon)=\int_0^{\varepsilon}\sigma(\tilde{\varepsilon})d\tilde{\varepsilon}=\frac{1}{2}E_0\varepsilon^2+\frac{1}{3}E_1\varepsilon^3 \tag{33}$$

The nonlinear constitutive relation is expanded in two dimensions as follows:

$$\begin{cases}\sigma_{11}=\dfrac{E_0}{(1+\nu)(1-2\nu)}\left[(1-\nu)\varepsilon_{11}+\nu\varepsilon_{22}\right]+E_1\left[\varepsilon_{11}^2+\mu(2\varepsilon_{11}\varepsilon_{22}+\varepsilon_{22}^2)\right]\\ \sigma_{12}=0\\ \sigma_{22}=\dfrac{E_0}{(1+\nu)(1-2\nu)}\left[(1-\nu)\varepsilon_{22}+\nu\varepsilon_{11}\right]+E_1\left[\varepsilon_{22}^2+\mu(2\varepsilon_{11}\varepsilon_{22}+\varepsilon_{11}^2)\right]\end{cases} \tag{34}$$

The nonlinear strain energy density is expanded in two dimensions as follows:

$$\begin{aligned}W_{CCM}&=\int_0^{\varepsilon}\sigma(\tilde{\varepsilon})d\tilde{\varepsilon}=\int_0^{\varepsilon_{liner}}\sigma_{liner}(\tilde{\varepsilon})d\tilde{\varepsilon}+\int_0^{\varepsilon_{nonliner}}\sigma_{nonliner}(\tilde{\varepsilon})d\tilde{\varepsilon}\\&=\frac{E_0}{2(1+\nu)(1-2\nu)}\left[(1-\nu)(\varepsilon_{11}^2+\varepsilon_{22}^2)+2\nu\varepsilon_{11}\varepsilon_{22}\right]+E_1\left[\frac{1}{3}(\varepsilon_{11}^3+\varepsilon_{22}^3)+\mu\left(\varepsilon_{11}^2\varepsilon_{22}+\varepsilon_{11}\varepsilon_{22}^2\right)\right]\end{aligned} \tag{35}$$

The parameter μ governs the nonlinear Poisson effect, while E_1 controls the nonlinear modulus. If the Poisson effect is neglected ($\nu=0$ and $\mu=0$), the strain energy density degenerates to $W=\frac{E_0}{2}(\varepsilon_{11}^2+\varepsilon_{22}^2)+\frac{E_1}{3}(\varepsilon_{11}^3+\varepsilon_{22}^3)$. Furthermore, when E_1 equals zero, the solution reverts to the classical linear elasticity.

The potential energy function for the PD bond is as follows:

$$W_{\mathrm{PD}}=\frac{1}{2}\int_{\mathrm{H_x}}c(s)s^2\,|\boldsymbol{\xi}|\,dA_{\mathbf{x}'} \tag{36}$$

Let $c(s)$ in the above formula be a polynomial:

$$c(s)=c_0+c_1 s \tag{37}$$

where c_0 governs the linear elastic response, c_1 introduces nonlinear elastic behavior. In the two-dimensional model, the bond stretch s can be written in terms of strain components as:

491 $$s = \varepsilon_r = \varepsilon_{11}\cos^2\theta + \varepsilon_{22}\sin^2\theta \tag{38}$$

492 Substituting Eq. (37) and (38) into Eq. (36) as follows:

493 $$\begin{aligned} W_{PD} &= \frac{1}{2}\int_H \frac{c(s)s^2}{2}|\boldsymbol{\xi}|dV_{x'} = \frac{1}{2}h\int_0^{\delta}\int_0^{2\pi}\frac{c(s)s^2}{2}|\boldsymbol{\xi}|\left(|\boldsymbol{\xi}|\right)d\theta d|\boldsymbol{\xi}| \\ &= \frac{h\delta^3}{12}\left[c_0\left(\frac{3\pi}{4}(\varepsilon_{11}^2+\varepsilon_{22}^2)+\frac{\pi}{2}\varepsilon_{11}\varepsilon_{22}\right)\right]+\frac{h\delta^3}{12}\left[c_1\left(\frac{5\pi}{8}(\varepsilon_{11}^3+\varepsilon_{22}^3)+\frac{3\pi}{8}(\varepsilon_{11}^2\varepsilon_{22}+\varepsilon_{11}\varepsilon_{22}^2)\right)\right] \end{aligned} \tag{39}$$

494 Combining Eq. (35) and (39), and applying $W_{CCM} = W_{\mathrm{PD}}$, we obtain: $c_0 = \frac{48E_0}{5\pi h\delta^3}$ and

495 $c_1 = \frac{32E_1}{5\pi h\delta^3}$.

496 The micro-modulus of the PD bond is obtained as a function of stretch:

497 $$c(s) = c_0 + c_1 s = \frac{48E_0}{5\pi h\delta^3} + \frac{32E_1}{5\pi h\delta^3}s \tag{40}$$

498 The nonlinear spring PD force is given as:

499 $$f_{nonlinear\_spring} = c(s)s = \frac{48E_0}{5\pi h\delta^3}s + \frac{32E_1}{5\pi h\delta^3}s^2 \tag{41}$$

500 **(2) Maxwell element**

501 The spring and dashpot in the Maxwell element are connected in series. The bond stretch s is

502 decomposed into elastic and viscous components:

503 $$s = s_e + s_v \tag{42}$$

504 The elastic and viscous bond forces in the series Maxwell element are equal, giving the

505 Maxwell bond force:

506 $$f_{Maxwell} = f_e = f_v \tag{43}$$

507 The linear spring of a single Maxwell element is embedded in PD, yielding the classical PD

508 equation as follows:

509 $$f_e = cs = \frac{48E}{5\pi h\delta^3}s_e \tag{44}$$

510 The dashpot component of the Maxwell element, given by Eq. (7) corresponds in classical

continuum mechanics to the following dissipation power density:

$$\mathrm{P}_{\mathrm{CCM}} = \frac{1}{2}\boldsymbol{\sigma}_{\mathrm{v}} : \dot{\boldsymbol{\varepsilon}} \tag{45}$$

The viscous stress $\boldsymbol{\sigma}_{\mathrm{v}}$ is given by:

$$\boldsymbol{\sigma}_{\mathrm{v}} = 2\eta_v \dot{\boldsymbol{\varepsilon}} + \lambda_v (\mathrm{tr}\dot{\boldsymbol{\varepsilon}})\boldsymbol{I} \tag{46}$$

Substituting Eq. (46) into Eq. (45) as follows:

$$\mathrm{P}_{\mathrm{CCM}} = \frac{1}{2}\left[\left(2\eta_v + \lambda_v\right)\left(\dot{\varepsilon}_{11}^2 + \dot{\varepsilon}_{22}^2\right) + 2\lambda_v \dot{\varepsilon}_{11}\dot{\varepsilon}_{22} \right] \tag{47}$$

where, η_v denotes the shear viscosity, reflecting resistance to shear deformation; λ_v represents the bulk viscosity, characterizing dissipation associated with compression or expansion.

Viscous effects are incorporated through the damping force f_v of the bond in peridynamics:

$$f_v = d_v \dot{s}_v \tag{48}$$

where d_v denotes the equivalent viscous stiffness of the bond, $\dot{s}$ is the time derivative of the bond stretch s.

The dissipation power density of a bond as follows:

$$\mathrm{P}_{\mathrm{bond}} = \frac{1}{2} f_v \cdot \dot{s}_v \cdot \xi = \frac{1}{2} d_v \dot{s}_v^2 \xi \tag{49}$$

Integral of contributions from all bonds within the PD horizon:

$$\begin{aligned} \mathrm{P}_{\mathrm{PD}} &= \frac{1}{2}\int_H \mathrm{P}_{\mathrm{bond}} dV_\xi = \frac{1}{2}\int_H \frac{1}{2} d_v \dot{s}_v^2 \xi dV_\xi \\ &= \frac{1}{2} h \int_0^{2\pi}\int_0^{\delta} \frac{1}{2} d_v \left(\dot{\varepsilon}_{11}^2 \cos^4\theta + \dot{\varepsilon}_{22}^2 \sin^4\theta + 2\dot{\varepsilon}_{11}\dot{\varepsilon}_{22}\cos^2\theta \sin^2\theta\right)\xi \cdot \xi d\xi d\theta \\ &= d_v h \frac{\pi\delta^3}{48}\left(3\dot{\varepsilon}_{11}^2 + 3\dot{\varepsilon}_{22}^2 + 2\dot{\varepsilon}_{11}\dot{\varepsilon}_{22}\right) \end{aligned} \tag{50}$$

Equating the PD dissipation power Eq. (50) with the classical continuum mechanics dissipation power Eq. (47) yields: $d_v = \dfrac{24\lambda_v}{h\pi\delta^3}$.

Thus, the Maxwell term in the PD equation as follows:

$$f_{Maxwell} = f_v = \frac{24\lambda_v}{h\pi\delta^3}\dot{s}_v \tag{51}$$

531 The damage is governed by the interactions of material points. If the bond stretch exceeds the
532 critical scopes, their interaction force vanishes, marking the damage appearance. Then damage
533 progressively accumulates, microcracks initially nucleate and gradually propagate, eventually
534 coalescing into macroscopic cracks.

535 The damage Ψ is written as the ratio of broken bonds to total bonds within its horizon, ranging
536 from 0 to 1.

537 $$\Psi\left(x,t\right)=1-\frac{\int_H \varphi\left(\boldsymbol{\xi},t\right)dV_{x'}}{\int_H dV_{x'}} \tag{52}$$

538 The bond status is written by the following function:

539 $$\varphi\left(\boldsymbol{\xi},t\right)=\begin{cases}1 & \text{if } s\left(\boldsymbol{\xi},t'\right)<s_0\\ 0 & \text{others}\end{cases} \tag{53}$$

540 The critical stretch s_0 is expressed in terms of the critical fracture energy G_0:

541 $$G_0=\int_H w_0\left(\boldsymbol{\eta},\boldsymbol{\xi}\right)dV_{x'}=\int_H \frac{cs_0{}^2}{2}\left|\boldsymbol{\xi}\right|dV_{x'} \tag{54}$$

542 The critical fracture energy of ice can be obtained either from direct experimental measurement
543 or derived from the fracture toughness K_I:

544 $$G_0=\frac{K_I{}^2}{E}\left(1-\nu^2\right) \tag{55}$$

545 The integral expression for the critical fracture energy of a two-dimensional ice borehole is
546 given by (Silling and Askari, 2005; Xu et al., 2024):

547 $$G_0=\int_H \frac{cs_0{}^2}{2}\left|\boldsymbol{\xi}\right|dV_{x'}=2h\int_0^{\delta}\int_z^{\delta}\int_0^{\arccos\left(\frac{z}{|\boldsymbol{\xi}|}\right)}\frac{cs_0{}^2}{2}\left|\boldsymbol{\xi}\right|\left(\left|\boldsymbol{\xi}\right|\right)d\varphi d\left|\boldsymbol{\xi}\right|dz=\frac{hc\delta^4}{4}s_0{}^2 \tag{56}$$

548 The critical stretch for the two-dimensional ice borehole is therefore:

549 $$s_0=\sqrt{\frac{4G_0}{hc\delta^4}}=\sqrt{\frac{4}{hc\delta^4}\frac{K_I{}^2}{E}\left(1-\nu^2\right)} \tag{57}$$

550 Substituting all of the above terms into the PD equation of motion Eq. (31), the complete PD

551 equation incorporating damage is obtained:

552 $$\rho(x)\ddot{\boldsymbol{u}}(x,t)=\int_H \varphi(\boldsymbol{\xi},t)\left(f_{nonlinear\_spring}+f_{Maxwell}\right)dV_{x'}+\boldsymbol{b}(x,t) \tag{58}$$

553 The numerical solution of PD equations uses a meshfree method. The integration over the PD

554 horizon is implemented through the following discretized scheme:

555 $$\rho(x_i)\ddot{\boldsymbol{u}}(x_i,t)=\sum_{j=1}^{N}\varphi_{ij}(\boldsymbol{\xi},t)\boldsymbol{f}\left(\boldsymbol{u}_j(x_j,t)-\boldsymbol{u}_i(x_i,t),x_j-x_i,t\right)V_j+\boldsymbol{b}(x_i,t) \tag{59}$$

556 To address quasi-static problems, the adaptive dynamic relaxation (ADR) technique is

557 implemented. This method introduces damping terms into peridynamic governing equations, as

558 follows:

559 $$\boldsymbol{D}\ddot{\boldsymbol{U}}(\boldsymbol{X},t)+z\boldsymbol{D}\dot{\boldsymbol{U}}(\boldsymbol{X},t)=\boldsymbol{F}(\boldsymbol{U},\boldsymbol{U}',\boldsymbol{X},\boldsymbol{X}') \tag{60}$$

560 where $\boldsymbol{D}$ is virtual mass, z denotes damping parameter, $\boldsymbol{X}$ corresponds to initial positions, $\boldsymbol{U}$

561 denotes initial displacements, and $\boldsymbol{F}$ includes both the PD interaction and the body force density.

562 The acceleration vector is approximated using a finite difference of displacements through the

563 explicit central difference scheme, as expressed below:

564 $$\boldsymbol{D}\frac{\dot{\boldsymbol{U}}^{n+\frac{1}{2}}-\dot{\boldsymbol{U}}^{n-\frac{1}{2}}}{\Delta t}+z^n\boldsymbol{D}\frac{\dot{\boldsymbol{U}}^{n+\frac{1}{2}}+\dot{\boldsymbol{U}}^{n-\frac{1}{2}}}{2}=\boldsymbol{F} \tag{61}$$

565 The velocity and displacement for the subsequent time step are determined by:

566 $$\dot{\boldsymbol{U}}^{n+\frac{1}{2}}=\frac{(2-z^n\Delta t)\dot{\boldsymbol{U}}^{n-\frac{1}{2}}+2\Delta t\boldsymbol{D}^{-1}\boldsymbol{F}^n}{2+z^n\Delta t} \tag{62}$$

567 $$\boldsymbol{U}^{n+1}=\boldsymbol{U}^n+\Delta t\dot{\boldsymbol{U}}^{n+\frac{1}{2}} \tag{63}$$

568 ## 4.5 Ice borehole fracturing

569 Ice borehole fracturing observed in polar drilling operations (Kuhl et al., 2021; Goodge et al.,

570 2021; Kudryashov et al., 2002; Vasilev et al., 2016; Talalay and Hong, 2021) are mainly caused by

571 overpressure and shock waves in the drilling fluid. Excessive pump pressure or fluid density may
572 induce hydraulic fracturing at borehole wall due to stress concentration (Chen et al., 2019). When
573 drill string is lowered quickly into the borehole, it pushes on the drilling fluid, causing the local
574 pressure to rise fast. This sudden pressure change may exceed the strength of ice wall, leading to
575 fractures and borehole instability. During the Rapid Access Ice Drill (RAID) test at Minna Bluff, ice
576 fracturing was observed at drilling fluid pressures as low as 0.52 MPa (Talalay and Hong, 2021),
577 highlighting the extreme sensitivity of ice to pressure fluctuations.

578 The Antarctic ice constitutive relation was embedded into the PD equations to analyze borehole
579 fracturing. The ice borehole is subjected to internal hydraulic and external horizontal loads. The
580 loading rates and PD parameters are listed in Table 3.

581 **Table 3.** PD parameters for ice borehole fracturing.

Model parameters	Values	Unit
Model domain	600	mm
Borehole radius	50	mm
Loading rate 1: hydraulic inside the hole	18.0	mm/min
Loading rate 1: horizontal	9.0	mm/min
Loading rate 2: hydraulic inside the hole	1.8	mm/min
Loading rate 2: horizontal	0.9	mm/min
Loading rate 3: hydraulic inside the hole	0.18	mm/min
Loading rate 3: horizontal	0.09	mm/min
Particle spacing	1.50	mm
Horizon	4.52	mm
Fracture Toughness	175	$kPa \cdot m^{0.5}$

582 Eight particle spacings Δx were tested: L/100, L/150, L/200, L/250, L/300, L/350, L/400, and

583 L/450, where L = 600 mm is the model size. Fig. 15 shows the displacement distribution under
584 internal and external boundary loading rates of 18 and 9 mm/min respectively, with a borehole radius
585 of 50 mm and a horizon of $3.015\Delta x$, PD numerical parameters as shown in Table 3.

586 The results show that when the particle spacing is refined to L/300, the displacement field
587 distribution stabilizes and further mesh refinement has negligible effect on the results. The particle
588 spacing adopted in this study is L/400 (1.50 mm), which lies within the convergence range, ensuring
589 computational accuracy while maintaining efficiency.

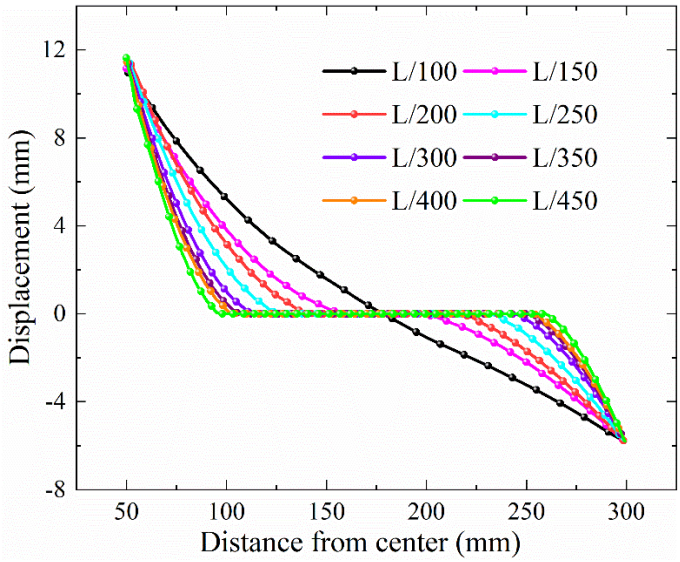

590

591 **Fig.** 15. Displacement curves from the center of the hole under different particle spacings

592 Fig. 16 illustrates the fracturing processes of ice boreholes under different loading rates,
593 categorized into four groups: high rate (18.0 and 9.0 mm/min), medium rate (1.8 and 0.9 mm/min),
594 low rate (0.18 and 0.09 mm/min), and extremely low rate (0.018 and 0.009 mm/min). The results
595 indicate that higher loading rates lead to greater strain rates in the ice borehole and faster fracturing,
596 with significant cracks forming in fewer steps (e.g., 80 steps). In contrast, lower rates result in slower
597 fracturing, requiring more steps (200, 1000, and 10,000, respectively) to observe noticeable changes.
598 As the number of time steps increases, the fracture patterns progressively develop and stabilize,

showing that the dynamic fracturing process of ice boreholes is highly dependent on both the loading rate and timescale.

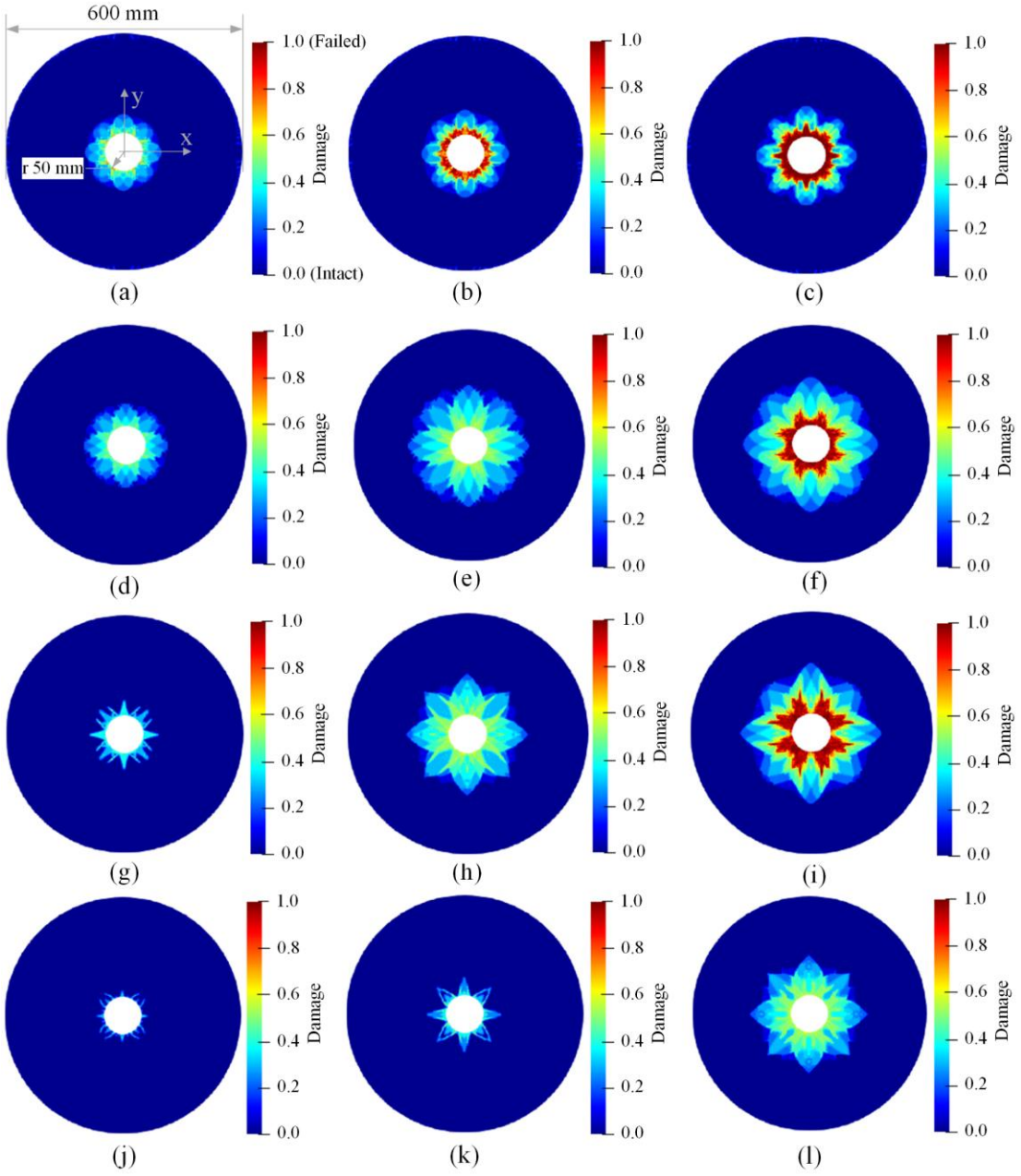

Fig. 16. Ice hole fracturing. (a) - (c): 40, 60 and 80 steps at internal and external boundary of 18.0 and 9.0 mm/min, (d) - (f): 100, 200 and 400 steps at internal and external boundary of 1.8 and 0.9 mm/min, (g) - (i): 200, 1000 and 2400 steps at internal and external boundary of 0.18 and 0.09 mm/min, (j) - (l): 1000, 2000 and 10000 steps at internal and external boundary of 0.018 and 0.009 mm/min.

606 The temporal evolution of damage ($\Psi > 0$), instability ($\Psi > 0.5$), and fragmentation ($\Psi > 0.8$)
607 areas under low loading rates, as shown in Fig. 17. The process can be divided into three stages: in
608 the initial stage, the damage area increases first while instability and fracture areas remain stable; in
609 the constant speed stage, damage continues to accumulate, instability begins to rise slowly, and
610 fragmentation remains minimal; in the acceleration stage, the growth rate of instability increases
611 markedly, accompanied by rapid fragmentation expansion. This three-stage evolution pattern
612 indicates that the failure of Antarctic ice under low loading rates exhibits a pronounced cumulative-
613 accelerative time effect. Once damage builds up to a critical point, it sets off a series of instability
614 and fragmentation events, leading to structural failure of the ice borehole.

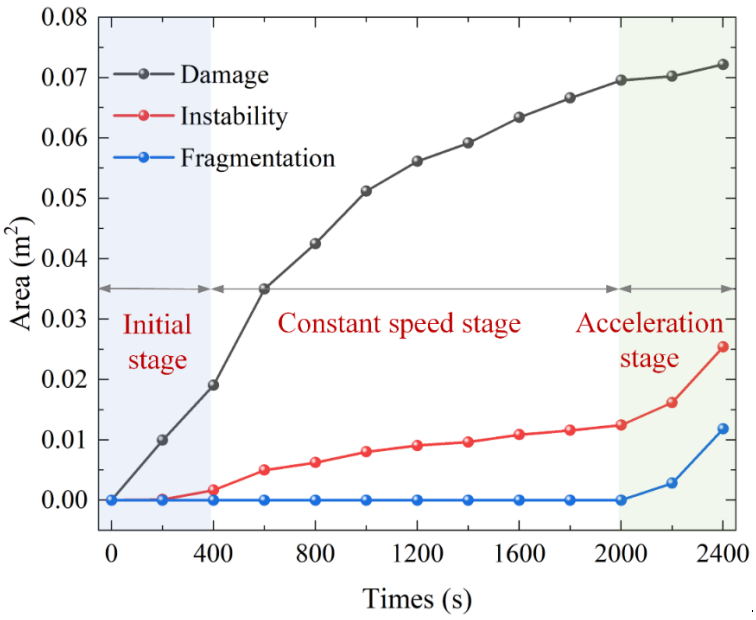

615

616 **Fig. 17.** Evolution process of damage, instability, and fragmentation area at internal and external loading
617 rate of 0.18 and 0.09 mm/min.

618 Fig. 18 shows the ratio of instability and fragmentation regions within the damaged under
619 different loading rates. The highest loading rate (Rate 1) exhibits the fastest increase in instability
620 proportion, which means that higher loading rates accelerate the instability development; the

instability growth rates for Rates 2 and 3 decrease, showing a clear rate dependence effect. Fragmentation occurring earlier under high loading conditions. The proportion of fragmentation goes down as the loading rate decreases. These findings show that higher loading rates leads to faster growth of instability and fragmentation within the damaged area. At the lower loading rate 3, the fragmentation ratio remains near zero throughout most of the loading process, indicating that the structural integrity of the borehole is maintained over a much longer period.

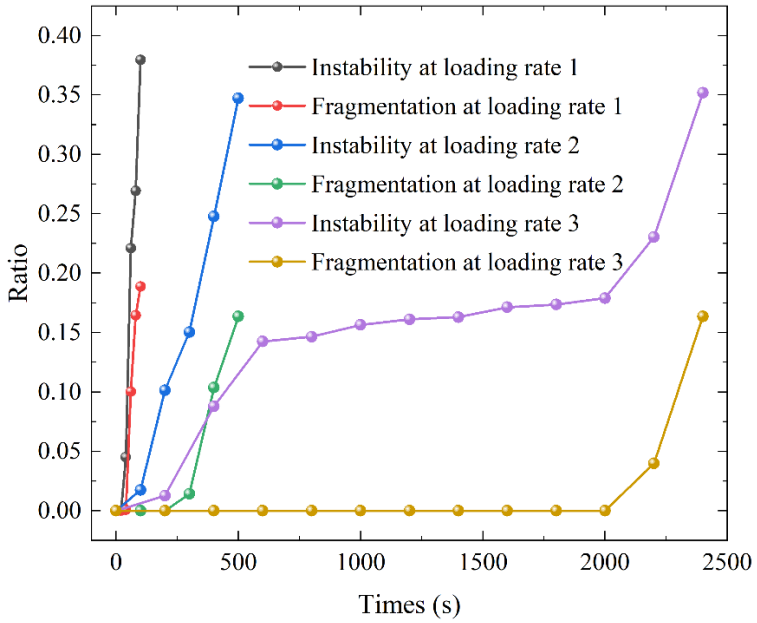

Fig. 18. Ratio of instability and fragmentation regions to the damaged under different loading rates.

The simulation results provide a quantitative basis for engineering recommendations regarding borehole pressure management. At the higher loading rate of 18.0 mm/min and 1.8 mm/min, significant macroscopic cracks appear within 60 and 200 steps, indicating rapid and catastrophic failure. In contrast, at the lower loading rate 0.18 mm/min, the damage evolution follows a pronounced three-stage pattern (Fig. 17): an initial stage where diffuse damage accumulates, a constant-speed stage where instability slowly develops, and an acceleration stage (after 2000 steps) where fragmentation rapidly expands. This three-stage behavior indicates that at the 0.18 mm/min

loading rate level, the ice borehole possesses a substantial damage buffer period before catastrophic failure, providing a critical time window for engineering intervention.

Theoretical analysis indicates that ice borehole fracturing is influenced not only by static pressure differentials but also by dynamic pressure fluctuations. Based on the above analysis, it is recommended that the ice borehole wall loading rate be controlled at less than 0.18 mm/min during polar drilling operations. Specific measures include: controlling the drill string descent speed, optimizing the drilling fluid pump pressure, and implementing pressure buffering devices to suppress transient pressure fluctuations induced by percussive shocks, as observed in the Agile Sub-Ice Geological (ASIG) drilling project (Kuhl et al., 2021). These measures ensure that the borehole remains in the damage accumulation stage rather than entering the instability or fragmentation stage, thereby preventing borehole fracturing and ensuring safe polar drilling operations.

5 Conclusions

This paper investigates the deformation and failure patterns of Antarctic ice through uniaxial and triaxial experiments conducted in a low-temperature laboratory, exploring the influence of loading rate, confining pressure, and temperature. We propose a constitutive model and analyze the failure characteristics of ice holes based on peridynamics. The conclusions are as follows:

The mechanical properties of Antarctic ice exhibit significant environmental sensitivity. The peak strength changes linearly with the loading rates. From 1.44 mm/min to 4.79 mm/min, the ultimate compressive strength increases by 108.77%. The Antarctic ice samples' failure exhibits a shear-tensile composite failure. As the loading rate increases, the Antarctic ice gradually transitions from shear to tensile failure.

A new constitutive model for Antarctic ice is proposed, effectively capturing strain-rate

sensitivity and time effects. Experimental results demonstrate that the model performs effectively over a wide range of strain rates, enhancing prediction accuracy by at least 5.36% compared to the improved Duncan-Chang model.

The proposed constitutive model is incorporated into peridynamics, revealing the rate-dependent behavior of ice borehole fracturing. High loading rates trigger rapid crack propagation, while low rates exhibit a typical three-stage damage accumulation. Suppressing pressure fluctuations and limiting the ice hole wall loading rate to less than 0.18 mm/min can delay damage and prevent borehole instability, providing guidance for safe drilling and structural design in polar and offshore engineering.

Due to the scarcity of Antarctic ice core samples, only a single specimen was tested for each experimental condition. The ranges of strain rate and temperature are limited and do not cover the long-term creep regime. The constitutive model has not yet been extended to 3D stress states. The 2D plane strain numerical model cannot capture axial damage propagation. Future work will focus on addressing these limitations, including establishing an Antarctic ice mechanics database through polar scientific expeditions, developing three-dimensional numerical models, and analyzing multi-physics coupled effects.

Declaration of Competing Interest

The authors declare that they have no known competing financial interests or personal relationships that could have appeared to influence the work reported in this paper.

Acknowledgments

The authors gratefully acknowledge the financial support from the National Key Research and Development Program of China (Grant No. 2023YFB3711705), Natural Science Foundation of

China (No. 42272362)， Key Laboratory of Polar Geology and Marine Mineral Resources (China University of Geosciences, Beijing), Ministry of Education（Number: HNPY-202412），Hainan Institute of China University of Geosciences, Beijing（Number: HNPY-202412） and Fundamental Research Funds for the Central Universities, China (No.379202408). We also thank the reviewers of the original manuscript, whose comments and suggestions helped to improve this paper.

Appendix A. Proof of thermodynamic consistency

The Helmholtz free energy density ψ is adopted as the thermodynamic potential to verify that the constitutive model satisfies the Clausius-Duhem inequality. The total free energy density consists of the elastic stored energy and the stored energy of each Maxwell branch:

$$\psi(\varepsilon,\varepsilon_{ks}) = \psi_{spring}(\varepsilon) + \sum_{k=1}^{n}\psi_k(\varepsilon_{ks}) \tag{A.1}$$

where ε_{ks} is the strain in the spring of the k^{th} Maxwell element.

The free energy of the nonlinear spring is defined as the path integral of stress over strain:

$$\psi_{spring}(\varepsilon) = \int_0^{\varepsilon}\sigma_{spring}(\xi)d\xi = \int_0^{\varepsilon}\left(E_{s0}\xi + E_{s1}\xi^2\right)d\xi = \frac{1}{2}E_{s0}\varepsilon^2 + \frac{1}{3}E_{s1}\varepsilon^3 \tag{A.2}$$

Eq. (A.2) can be directly verified that:

$$\frac{\partial\psi_{spring}}{\partial\varepsilon} = E_{s0}\varepsilon + E_{s1}\varepsilon^2 = \sigma_{spring}(\varepsilon) \tag{A.3}$$

The stored energy of the k^{th} Maxwell spring is:

$$\psi_k(\varepsilon_{ks}) = \frac{1}{2}E_k\varepsilon_{ks}^2 \tag{A.4}$$

$$\frac{\partial\psi_k}{\partial\varepsilon_{ks}} = E_k\varepsilon_{ks} = \sigma_{ks} = \sigma_k \tag{A.5}$$

Taking the material time derivative of the total free energy Eq. (A.1) and applying the chain rule:

$$\dot{\psi} = \frac{\partial \psi_{spring}}{\partial \varepsilon}\dot{\varepsilon} + \sum_{k=1}^{n} \frac{\partial \psi_k}{\partial \varepsilon_{ks}}\dot{\varepsilon}_{ks} = \sigma_{spring}\dot{\varepsilon} + \sum_{k=1}^{n} \sigma_k \dot{\varepsilon}_{ks} \tag{A.6}$$

The first term represents the power input to the nonlinear spring, which is entirely converted into reversible stored energy. The second term represents the rate of energy storage in each Maxwell spring.

The Clausius-Duhem inequality requires that the mechanical dissipation satisfies:

$$D = \sigma\dot{\varepsilon} - \dot{\psi} \geq 0 \tag{A.7}$$

Substituting the expression for $\dot{\psi}$:

$$D = \sigma\dot{\varepsilon} - \sigma_{spring}\dot{\varepsilon} - \sum_{k=1}^{n} \sigma_k \dot{\varepsilon}_{ks} \tag{A.8}$$

Substituting the stress superposition $\sigma = \sigma_{spring} + \sum_{k=1}^{n} \sigma_k$:

$$D = \left(\sigma_{spring} + \sum_{k=1}^{n} \sigma_k \right)\dot{\varepsilon} - \sigma_{\text{spring}}\dot{\varepsilon} - \sum_{k=1}^{n} \sigma_k \dot{\varepsilon}_{ks} \tag{A.9}$$

The $\sigma_{\text{spring}}\dot{\varepsilon}$ terms cancel, reflecting that the power input to the nonlinear spring is entirely equal to its free energy increment. The spring branch is strictly reversible and dissipation-free. The expression simplifies to:

$$D = \sum_{k=1}^{n} \sigma_k (\dot{\varepsilon} - \dot{\varepsilon}_{ks}) \tag{A.10}$$

From the Maxwell strain decomposition $\varepsilon = \varepsilon_{ks} + \varepsilon_{kv}$, taking the time derivative:

$$\dot{\varepsilon} - \dot{\varepsilon}_{ks} = \dot{\varepsilon}_{kv} \tag{A.11}$$

Then

$$D = \sum_{k=1}^{n} \sigma_k \dot{\varepsilon}_{kv} \tag{A.12}$$

This shows that the total dissipation power is strictly equal to the sum of the products of the

dashpot stress σ_k and dashpot strain rate $\dot{\varepsilon}_{kv}$ in each Maxwell element. The nonlinear spring contributes no dissipation, nor do the Maxwell springs. All dissipation arises entirely from viscous flow in the dashpots.

Substituting the dashpot constitutive relation $\sigma_k = \sigma_{kv} = \eta_k \dot{\varepsilon}_{kv}$:

$$D = \sum_{k=1}^{n} \left(\eta_k \dot{\varepsilon}_{kv}\right) \cdot \dot{\varepsilon}_{kv} = \sum_{k=1}^{n} \eta_k \left(\dot{\varepsilon}_{kv}\right)^2 \tag{A.13}$$

Since $\eta_k > 0$ and $\dot{\varepsilon}_{kv}{}^2 \geq 0$, the total dissipation $D \geq 0$ holds strictly for any strain history and at any time instant.

Equality holds if and only if $\dot{\varepsilon}_{kv} = 0$ $(k = 1, \ldots, n)$, all dashpots are at rest. In this limit, the system degenerates into a purely elastic response, with the nonlinear spring and all Maxwell springs jointly carrying the load and no viscous flow occurring. This limiting case is fully consistent with physical expectations.

References

Askari, E., Bobaru, F., Lehoucq, R.B., Parks, M.L., Silling, S.A., Weckner, O., 2008. Peridynamics for multiscale materials modeling. J. Phys. Conf. Ser. 125, 12078. https://doi.org/10.1088/1742-6596/125/1/012078

Bailey, E., Taylor, R., Croasdale, K.R., 2015. Mechanics of ice rubble over multiple scales, in: Omae2015. Volume 8: Ian Jordaan Honoring Symposium on Ice Engineering. https://doi.org/10.1115/OMAE2015-42004

Chen, C., Zhang, H., Liu, S., Jin, C., Chen, Y., Zhang, N., Talalay, P., 2019. Hydraulic fracturing in ice boreholes: theory and tests. Polar Sci. 19, 40–48. https://doi.org/10.1016/j.polar.2018.10.003

Dansereau, V., Weiss, J., Saramito, P., Lattes, P., 2016. A maxwell elasto-brittle rheology for sea ice modelling. The Cryosphere 10, 1339–1359. https://doi.org/10.5194/tc-2015-200

Fourteau, K., Gillet-Chaulet, F., Martinerie, P., Faïn, X., 2020. A micro-mechanical model for the transformation of dry polar firn into ice using the level-set method. Front. Earth Sci. 8. https://doi.org/10.3389/feart.2020.00101

Freitag, J., Wilhelms, F., Kipfstuhl, S., 2004. Microstructure-dependent densification of polar firn derived from X-ray microtomography. J. Glaciol. 50, 243–250. https://doi.org/10.3189/172756504781830123

Gagnon, R.E., 2011. A numerical model of ice crushing using a foam analogue. Cold Reg. Sci. Technol. 65, 335–350. https://doi.org/10.1016/j.coldregions.2010.11.004

Gagnon, R.E., Wang, J., 2012. Numerical simulations of a tanker collision with a bergy bit incorporating hydrodynamics, a validated ice model and damage to the vessel. Cold Reg. Sci. Technol. 81, 26–35. https://doi.org/10.1016/j.coldregions.2012.04.006

Girard, L., Bouillon, S., Weiss, J., Amitrano, D., Fichefet, T., Legat, V., 2011. A new modeling framework for sea-

ice mechanics based on elasto-brittle rheology. Ann. Glaciol. 52, 123–132. https://doi.org/10.3189/172756411795931499

Glen, J.W., 1955. The creep of polycrystalline ice. Proc. R. Soc. Lond. Math. Phys. Sci. 228, 519–538. https://doi.org/10.1098/rspa.1955.0066

Goldsby, D.L., Kohlstedt, D.L., 2001. Superplastic deformation of ice: experimental observations. J. Geophys. Res. Solid Earth 106, 11017–11030. https://doi.org/10.1029/2000JB900336

Goodge, J.W., Severinghaus, J.P., Johnson, J., Tosi, D., Bay, R., 2021. Deep ice drilling, bedrock coring and dust logging with the rapid access ice drill (RAID) at minna bluff, antarctica. Ann. Glaciol. 62, 324–339. https://doi.org/10.1017/aog.2021.13

Han, D., Lee, H., Choung, J., Kim, H., Daley, C., 2017. Cone ice crushing tests and simulations associated with various yield and fracture criteria. Ships Offshore Struct. 12, S88–S99. https://doi.org/10.1080/17445302.2016.1266920

Hjort, J., Streletskiy, D., Doré, G., Wu, Q., Bjella, K., Luoto, M., 2022. Impacts of permafrost degradation on infrastructure. Nat. Rev. Earth Environ. 3, 24–38. https://doi.org/10.1038/s43017-021-00247-8

Ince, S.T., Kumar, A., Paik, J.K., 2017. A new constitutive equation on ice materials. Ships Offshore Struct. 12, 611–623. https://doi.org/10.1080/17445302.2016.1190122

Javili, A., Morasata, R., Oterkus, E., Oterkus, S., 2019. Peridynamics review. Math. Mech. Solids 24, 3714–3739. https://doi.org/10.1177/1081286518803411

Kim, J.-H., Kim, Y., 2019. Numerical simulation of concrete abrasion induced by unbreakable ice floes. Int. J. Nav. Archit. Ocean Eng. 11, 59–69. https://doi.org/10.1016/j.ijnaoe.2018.01.003

Kudryashov, B.B., Vasiliev, N.I., Vostretsov, R.N., Dmitriev, A.N., Zubkov, V.M., Krasilev, A.V., Talalay, P.G., Barkov, N.I., Lipenkov, V.Y., Petit, J.R., 2002. Deep ice coring at vostok station (east Antarctica) by an electromechanical drill. Mem. Natl. Inst. Polar Res. Spec. Issue 56, 91–102.

Kuhl, T., Gibson, C., Johnson, J., Boeckmann, G., Moravec, E., Slawny, K., 2021. Agile sub-ice geological (ASIG) drill development and pirrit hills field project. Ann. Glaciol. 62, 53–66. https://doi.org/10.1017/aog.2020.59

Liang, G., Xiao, E., Dong, X., Tang, X., Hu, B., Zhang, Z., Sun, B., 2025. Mechanical properties of antarctic blue ice: effects of strain rate and temperature on strength parameters. Constr. Build. Mater. 489, 142178. https://doi.org/10.1016/j.conbuildmat.2025.142178

Litwin, K.L., Zygielbaum, B.R., Polito, P.J., Sklar, L.S., Collins, G.C., 2012. Influence of temperature, composition, and grain size on the tensile failure of water ice: implications for erosion on titan. J. Geophys. Res. Planets 117. https://doi.org/10.1029/2012je004101

Lou, X., Wu, Y., 2021. Splitting tensile mechanical properties of plain ice and fiber - reinforced ice. Cold Reg. Sci. Technol. 192, 103381. https://doi.org/10.1016/j.coldregions.2021.103381

Lv, X., Cui, Z., Wang, T., Wen, Y., Liu, A., Wang, R., 2024. Research into mechanical modeling based on characteristics of the fracture mechanics of ice cutting for scientific drilling in polar regions. The Cryosphere 18, 3351–3362. https://doi.org/10.5194/tc-18-3351-2024

Marchenko, A., Morozov, E., Muzylev, S., 2013. Measurements of sea-ice flexural stiffness by pressure characteristics of flexural-gravity waves. Ann. Glaciol. 54, 51–60. https://doi.org/10.3189/2013aog64a075

Mohapatra, S.C., Amouzadrad, P., Soares, C.G., 2025. Recent developments in the nonlinear hydroelastic modeling of sea ice interaction with marine structures. J. Mar. Sci. Eng. 13. https://doi.org/10.3390/jmse13081410

Mokhtari, M., Leira, B.J., 2024. A critical review of constitutive models applied to ice-crushing simulations. J. Mar. Sci. Eng. 12, 1021. https://doi.org/10.3390/jmse12061021

Obisesan, A., Sriramula, S., 2018. Efficient response modelling for performance characterisation and risk assessment

of ship-iceberg collisions. Appl. Ocean Res. 74, 127–141. https://doi.org/10.1016/j.apor.2018.03.003
Qiu, W., Peng, R., 2021. Research on the numerical simulation for plastic model of ice as building materials under triaxial compression. Constr. Build. Mater. 268, 121183. https://doi.org/10.1016/j.conbuildmat.2020.121183
Rist, M.A., Murrell, S.A.F., 1994. Ice triaxial deformation and fracture. J. Glaciol. 40, 305–318. https://doi.org/10.3189/s0022143000007395
Shan, R.L., Bai, Y., Sui, S.M., Yang, H., Duan, J.M., 2018. Experimental research on mechanical characteristics of freshwater ice under triaxial compression. J Basic Sci Eng 26, 901–17. https://doi.org/10.16058/j.issn.1005-0930.2018.04.019
Silling, S.A., 2000. Reformulation of elasticity theory for discontinuities and long-range forces. J. Mech. Phys. Solids 48, 175–209. https://doi.org/10.1016/S0022-5096(99)00029-0
Silling, S.A., Askari, E., 2005. A meshfree method based on the peridynamic model of solid mechanics. Comput. Struct. 83, 1526–1535. https://doi.org/10.1016/j.compstruc.2004.11.026
Silling, S. A., Askari, E., 2005. A meshfree method based on the peridynamic model of solid mechanics. Comput. Struct., Advances in Meshfree Methods 83, 1526–1535. https://doi.org/10.1016/j.compstruc.2004.11.026
Skatulla, S., Audh, R.R., Cook, A., Hepworth, E., Johnson, S., Lupascu, D.C., MacHutchon, K., Marquart, R., Mielke, T., Omatuku, E., Paul, F., Rampai, T., Schröder, J., Schwarz, C., Vichi, M., 2022. Physical and mechanical properties of winter first-year ice in the antarctic marginal ice zone along the good hope line. The Cryosphere 16, 2899–2925. https://doi.org/10.5194/tc-16-2899-2022
Snyder, S.A., Schulson, E.M., Renshaw, C.E., 2016. Effects of prestrain on the ductile-to-brittle transition of ice. Acta Mater. 108, 110–127. https://doi.org/10.1016/j.actamat.2016.01.062
Talalay, P.G., Hong, J., 2021. Perspectives for development of ice drilling technology: continuation of the discussion. Ann. Glaciol. 62, 143–156. https://doi.org/10.1017/aog.2020.81
Timco, G.W., Weeks, W.F., 2010. A review of the engineering properties of sea ice. Cold Reg. Sci. Technol. 60, 107–129. https://doi.org/10.1016/j.coldregions.2009.10.003
Vasilev, N.I., Dmitriev, A.N., Podoliak, A.V., Lukin, V.V., Turkeev, A.V., 2016. Maintaining differential pressure in boreholes drilled in ice and the effect of ice hydrofracturing. Int. J. Appl. Eng. Res. 11, 9740–9747.
Wang, Y, Chen, G., Wan, B., Cai, G., & Zhang, Y. (2020). Behavior of circular ice-filled self-luminous FRP tubular stub columns under axial compression. *Construction and Building Materials*, *232*, 117287. https://doi.org/10.1016/j.conbuildmat.2019.117287
Wang, Y, Chen, G., Wan, B., Lin, H., & Zhang, J. (2018). Behavior of innovative circular ice filled steel tubular stub columns under axial compression. *Construction and Building Materials*, *171*, 680–689. https://doi.org/10.1016/j.conbuildmat.2018.03.208
Xu, H., Liu, Y., He, C., Hou, Z., Yang, G., 2024. Hydraulic fracture characterization of debris-rich ice hole for polar geological drilling based on Peridynamics. Ocean Eng. 306, 118116. https://doi.org/10.1016/j.oceaneng.2024.118116
Xu, H., Liu, Y., Hou, Z., Dou, Z., Zhang, J., Yang, G., 2023. Study on hydraulic cracking mechanism and propagation characteristics of ice hole based on Peridynamics. Appl. Ocean Res. 139, 103719. https://doi.org/10.1016/j.apor.2023.103719
Xu, N., Yuan, S., Liu, X., Ma, Y., Shi, W., Zhang, D., 2020. Risk assessment of sea ice disasters on fixed jacket platforms in liaodong bay. Nat. Hazards Earth Syst. Sci. 20, 1107–1121. https://doi.org/10.5194/nhess-20-1107-2020
Zhang, J., Wang, X., Sun, K., Lai, Y., Gao, D., Kang, W.-H., Wang, Bin, Wang, Bingjun, 2023. Ice-induced vibration analysis of offshore platform structures based on cohesive element method. J. Mar. Sci. Eng. 12.

https://doi.org/10.3390/jmse12010028
Zhang, W., Li, J., Li, L., Yang, Q., 2022. A systematic literature survey of the yield or failure criteria used for ice material. Ocean Eng. 254, 111360. https://doi.org/10.1016/j.oceaneng.2022.111360
Zhang, Y., Wang, Q., Han, D., Xue, Y., Lu, S., Wang, P., 2020. Dynamic splitting tensile behaviours of distilled-water and river-water ice using a modified SHPB setup. Int. J. Impact Eng. 145, 103686. https://doi.org/10.1016/j.ijimpeng.2020.103686